

# Analysis of Cloud-Resolving Model Simulations for Scale Dependence of Convective Momentum Transport

YI-CHIN LIU

*Pacific Northwest National Laboratory, Richland, Washington, and Air Resources Board, California Environmental Protection Agency, Sacramento, California*

JIWEN FAN

*Pacific Northwest National Laboratory, Richland, Washington*

KUAN-MAN XU

*NASA Langley Research Center, Hampton, Virginia*

GUANG J. ZHANG

*Scripps Institution of Oceanography, University of California, San Diego, La Jolla, California*

(Manuscript received 15 January 2018, in final form 12 April 2018)

## ABSTRACT

We use 3D cloud-resolving model (CRM) simulations of two mesoscale convective systems at midlatitudes and a simple statistical ensemble method to diagnose the scale dependency of convective momentum transport (CMT) and CMT-related properties and evaluate a parameterization scheme for the convection-induced pressure gradient (CIPG) developed by Gregory et al. Gregory et al. relate CIPG to a constant coefficient multiplied by mass flux and vertical mean wind shear. CRM results show that mass fluxes and CMT exhibit strong scale dependency in temporal evolution and vertical structure. The upgradient-downgradient CMT characteristics for updrafts are generally similar between small and large grid spacings, which is consistent with previous understanding, but they can be different for downdrafts across wide-ranging grid spacings. For the small to medium grid spacings (4–64 km), Gregory et al. reproduce some aspects of CIPG scale dependency except for underestimating the variations of CIPG as grid spacing decreases. However, for large grid spacings (128–512 km), Gregory et al. might even less adequately parameterize CIPG because it omits the contribution from either the nonlinear-shear or the buoyancy forcings. Further diagnosis of CRM results suggests that inclusion of nonlinear-shear forcing in Gregory et al. is needed for the large grid spacings. For the small to median grid spacings, a modified Gregory et al. with the three-updraft approach help better capture the variations of CIPG as grid spacing decreases compared to the single updraft approach. Further, the optimal coefficients used in Gregory et al. seem insensitive to grid spacings, but they might be different for updrafts and downdrafts, for different MCS types, and for zonal and meridional components.

## 1. Introduction

Convective momentum transport (CMT), which refers to transport of horizontal momentum in the vertical

direction by cumulus clouds, occurs mostly in the troposphere and has been demonstrated to have an essential impact on global atmospheric circulations and climate in both observational and numerical studies (e.g., Houze 1973; LeMone 1983; Helfand 1979; Zhang and McFarlane 1995; Song et al. 2008; Richter and Rasch 2008; Majda and Stechmann 2008, 2009, 2016; Khouider et al. 2012a,b; Shaw and Lane 2013; Lane and Moncrieff 2010; Moncrieff and Liu 2006; Badlan et al. 2017). However, it is a challenging task to fully understand CMT and parameterize it

---

Supplemental information related to this paper is available at the Journals Online website: <https://doi.org/10.1175/JAS-D-18-0019.s1>.

---

Corresponding author: Jiwen Fan, [jiwen.fan@pnnl.gov](mailto:jiwen.fan@pnnl.gov)

DOI: 10.1175/JAS-D-18-0019.1

© 2018 American Meteorological Society. For information regarding reuse of this content and general copyright information, consult the [AMS Copyright Policy \(www.ametsoc.org/PUBSReuseLicenses\)](https://www.ametsoc.org/PUBSReuseLicenses).

because 1) CMT cannot be directly measured on a global scale and instead is estimated as a residual from the small imbalance between the large-scale horizontal pressure gradient force (PGF) and the Coriolis force from intensive field experiments (Sui and Yanai 1986; Wu and Yanai 1994; Tung and Yanai 2002a,b), 2) CMT is not a conserved variable and comprises two horizontal components that can behave differently for different mesoscale convective systems (MCSs; Asai 1970; LeMone 1983; LeMone and Jorgensen 1991; Wu and Arakawa 2014), and 3) CMT has multiscale features ranging from cloud clusters on mesoscale to convectively coupled equatorial waves (CCW) on equatorial synoptic scales (Majda and Stechmann 2009; Khouider et al. 2012a,b).

Most observational data and theoretical studies suggest that CMT is often downgradient in nonlinear MCSs and can be either upgradient or downgradient for linear MCSs (Moncrieff and Green 1972; LeMone et al. 1984; Moncrieff 1992; Grabowski and Moncrieff 2001; Khouider et al. 2012b; Majda and Stechmann 2009). For nonlinear MCSs, such as mesoscale convective complex (MCC), Sui and Yanai (1986) and Tollerud and Esbensen (1983) utilized data from phase III of Global Atmospheric Research Program (GARP) Atlantic Tropical Experiment (GATE) and discovered that nonlinear MCSs tend to decelerate the large-scale flow in the upper troposphere as well as reduce the vertical wind shear in the lower troposphere. Therefore, CMT is downgradient with respect to mean wind shear. Wu and Yanai (1994) found that CMT is downgradient in the upper troposphere for MCC using observation data from the Oklahoma–Kansas Preliminary Regional Experiment for STORM-Central (OK PRE-STORM) and Atmospheric Variability Experiment–Severe Environmental Storms and Mesoscale Experiment (SESAME).

For linear MCSs, Asai (1970), LeMone (1983), Gallus and Johnson (1992), and Wu and Yanai (1994) have consistently shown that the line-parallel component of CMT is downgradient, but the line-normal component of CMT is upgradient. LeMone and Jorgensen (1991) reported that for cloud systems during the Taiwan Area Mesoscale Experiment, the line-normal component of CMT is downgradient in the lower troposphere but becomes upgradient in the upper troposphere. Zhang and Wu (2003) used 2D cloud-resolving model (CRM) to study the CMT of tropical convection observed during the Tropical Ocean and Global Atmosphere Coupled Ocean–Atmosphere Response Experiment intensive observation period, and they pointed out that the CMT in the easterly wind regime is downgradient, but CMT in the westerly wind burst is upgradient. Houze et al.

(2000) uses Doppler radar data collected by aircraft and ship and found that CMT was downgradient within the westerly onset region and was upgradient within the westerly wind burst. Khouider et al. (2012b) employed a multcloud model and suggested that CMT associated with CCW in front of the Madden–Julian oscillation (MJO) is downgradient, while the CMT associated the squall lines east of the convection core is upgradient.

Many studies have attempted to parameterize the effect of CMT in general circulation models (GCMs; e.g., Schneider and Lindzen 1976, hereafter SL76; Zhang and McFarlane 1995; Gregory et al. 1997, hereafter GKI97). Despite the complexity of CMT, this effect is often formulated in a grossly simplified way. In the early years of CMT parameterization development, CMT was parameterized in a simplified form by assuming that in-cloud horizontal momentum depends only on lateral detrainment and entrainment rates (Ooyama 1971; SL76). However, since LeMone (1983) and LeMone et al. (1984) demonstrated that in-cloud horizontal momentum can also be strongly influenced by the convection-induced pressure gradient (CIPG) using observational data from field experiments, many studies attempted to include the effects of CIPG on in-cloud momentum in their CMT parameterization schemes (Zhang and Cho 1991a,b, hereafter ZC91; Wu and Yanai 1994; GKI97). To include the CIPG effect in the CMT parameterization, ZC91 parameterized CIPG in terms of cloud-scale circulation and the interaction between convective updrafts/downdrafts and vertical mean wind shear. Wu and Yanai (1994) and GKI97 represented the CIPG by assuming that it is proportional to the product of cloud mass flux and vertical mean wind shear. Cheng and Xu (2014) parameterized the CIPG effect by using a multiscale modeling framework (MMF), which is also known as superparameterization (Khairoutdinov and Randall 2001). MMF consists of a 2D CRM embedded in each grid column of GCM, which can explicitly treat cloud-scale processes. The embedded CRM in the MMF provides vertical transport of momentum in one horizontal direction, while in the other direction, the vertical momentum transport is assumed to be proportional to the vertical mass flux diagnosed from the CRM in addition to the effects of entrainment and detrainment. To represent both upgradient and downgradient vertical momentum transports, the orientation of the 2D CRM varies with time, which is determined by the stratification of the lower troposphere and environmental wind shear. Tulich (2015) also developed a similar CMT parameterization scheme as Cheng and Xu (2014) for the Weather Research and

Forecasting (WRF) Model, which is referred to as the superparameterized version of the Weather Research and Forecasting Model (SP-WRF). The SP-WRF can directly calculate the CIPG and CMT by using information obtained from a 2D CRM with periodic lateral boundary.

Different from the aforementioned mixing-entrainment CMT parameterization schemes, [Moncrieff \(1981, 1992\)](#) parameterize the CMT effects by specifically considering the entire cumulus clouds and associated mesoscale circulation. They used analytical models to represent major flow patterns of squall lines, which allowed their parameterization scheme to capture the upgradient and downgradient features of CMT ([LeMone and Moncrieff 1994](#)). However, this analytical model requires several parameters such as the depth of the cloud and the detailed mesoscale flow pattern, which are not available in most of the GCMs. This limits the applicability of this scheme in conventional GCMs with parameterized physical processes.

One of the disadvantages of typical mixing-entrainment CMT parameterization schemes (e.g., [SL76](#); [GKI97](#); [ZC91](#)) is requiring expensive computational resources. To provide cheaper alternatives, many studies have proposed different methods to parameterize CMT effects ([Majda and Stechmann 2008, 2009, 2016](#); [Khouider et al. 2012a,b](#)). [Majda and Stechmann \(2008, 2009\)](#) developed a simple stochastic model based on weak temperature gradient (WTG) approximation as well as a simple dynamic model, both of which are able to capture the important features of CMT, including both upgradient and downgradient transport of CMT. [Khouider et al. \(2012a\)](#) developed an even simpler model to handle the upgradient and downgradient feature of CMT by using a similar approach to [Majda and Stechmann \(2008\)](#) but replaced the stochastic process with a simple exponential distribution function.

Using CMT parameterizations in GCMs has greatly improved the simulations and forecasting of large-scale circulations. For example, [Helfand \(1979\)](#) found an enhanced winter Hadley circulation and more realistic simulated meridional winds when using a simple [SL76](#) CMT scheme in the Goddard Laboratory for Atmospheric Sciences (GLAS) GCM model. [Zhang and McFarlane \(1995\)](#) obtained similar results to [Helfand \(1979\)](#) when including the [ZC91](#) CMT parameterization in the Canadian Centre for Climate Modelling and Analysis model. [Wu et al. \(2003\)](#) successfully captured the seasonal migration of the intertropical convergence zone (ITCZ) precipitation when the [ZC91](#) CMT scheme was included in the

National Center for Atmospheric Research Community Climate System Model, version 3 (CCSM3). [Cheng and Xu \(2014\)](#) showed that the stationary anomalous precipitation can be reduced and more realistic large-scale circulation can be obtained when using their CMT parameterization scheme in the superparameterized Community Atmosphere Model (SPCAM), version 3.5. [Tulich \(2015\)](#) obtained improvement of tropical wave variability and the global simulations of seasonal climate when using his proposed CMT scheme in the WRF Model. Hurricane intensity forecasting also showed promising improvement with the inclusion of the [GKI97](#) CMT scheme in NCEP's operational Global Forecast System (GFS) and its nested regional spectral model because the CMT scheme can effectively suppress spurious weak tropical disturbances ([Han and Pan 2006](#)). [Deng and Wu \(2010\)](#) also obtained a more coherent structure for the MJO deep convective center and its corresponding atmospheric variances when including a CMT scheme in the Iowa State University (ISU) GCM.

[Richter and Rasch \(2008\)](#) and [Romps \(2012\)](#) further compared two mixing-entrainment CMT schemes with and without CIPG. Both studies found that using the [GKI97](#) scheme resulted in less improvement in the simulated large-scale circulations than using the [SL76](#) scheme even though the [GKI97](#) scheme was more physically representative than the [SL76](#) scheme. One of the potential attributions of poorer performance of the [GKI97](#) scheme is the high uncertainty in setting the coefficients in the formulation of CIPG. This uncertainty has been reflected in the past studies in which different coefficients have been adopted, such as 0.7 by [GKI97](#) and [Richter and Rasch \(2008\)](#), 0.55 by [Zhang and Wu \(2003\)](#), and 0.4 in CAM, version 5.1 (CAM5.1; [Neale et al. 2010](#)). In addition, the same coefficient has been used for both the zonal and meridional components of updraft and downdraft CIPG.

With increasing computing power, GCMs and regional climate models are able to run in a wide range of horizontal resolutions from hundreds of kilometers to a few kilometers. The aforementioned uncertainties may be amplified at higher spatial resolutions because of the lack of understanding of the scale dependency of CMT and CIPG. Improving this understanding is required to further improve CMT parameterizations, especially for the scale-adaptable aspects ([Liu et al. 2015](#)). Since the [GKI97](#) scheme is one of the widely used CMT schemes in GCMs, it is important to reevaluate the performance of the [GKI97](#) scheme and explore its adaptability to model resolution.

This study expands on the work of Zhang and Wu (2003), with the focus on diagnosing and exploring the scale dependency of CMT and CMT-related properties and evaluating the CIPG parameterization in the GK197 scheme. Instead of using 2D CRM simulations as in Zhang and Wu (2003), we utilize 3D WRF Model simulations with explicit spectral-bin microphysics (SBM) at the cloud-permitting scale for midlatitude convective cloud systems (Fan et al. 2015). The scale dependency of CMT and CMT-related properties will be diagnosed using a simple statistical ensemble method that was proposed by Arakawa et al. (2011), Arakawa and Wu (2013), and Wu and Arakawa (2014) and modified by Liu et al. (2015). The main goal of this study is twofold: 1) to explore the scale dependencies of mass flux, CMT, and CIPG for the midlatitude convective cloud systems and 2) to evaluate the formulation for parameterizing CIPG in the GK197 scheme for different grid spacings.

## 2. Case description and CRM simulations

CMT can be different between MCCs and squall lines. To investigate the scale dependencies of CMT for both linear and nonlinear systems, one MCC case and one squall line case over the midlatitude continent are selected for the CRM simulations. The two convection cases are from the Midlatitude Continental Convective Clouds Experiment (MC3E) near the DOE ARM Southern Great Plains (SGP) site (Petersen and Jensen 2012).

The simulations for the two cases are conducted using the Advanced Research version of WRF, version 3.3.1, using the SBM (Khain et al. 2004; Fan et al. 2012) with open lateral boundaries. The SBM is an advanced microphysics scheme solving the microphysical processes explicitly based on the predicted particles over a number of size bins. It has more physical representations of microphysical processes compared with 1-moment and 2-moment bulk schemes, particularly in the hydrometeor diffusional growth and subcloud rain evaporation, as discussed in Wang et al. (2013). The detailed description of cases and the model simulations have been presented in Fan et al. (2015). Briefly, two cases have a horizontal domain size of  $560 \times 560 \text{ km}^2$  with  $1 \times 1 \text{ km}^2$  horizontal grid spacing and save model outputs every 6 min. The number of model vertical layers are 41 for MC3E-0523 and 45 for MC3E-0520. Liu et al. (2015) analyzed convective moisture transport. In this study, our analyses are also based on the same simulations. The analysis time period is 6 h for MC3E-0523 and 4 h for MC3E-0520.

## 3. Methodology

A simple statistical ensemble method presented by Arakawa et al. (2011), Arakawa and Wu (2013), and Wu and Arakawa (2014) and modified by Liu et al. (2015) is used to examine the scale dependency of CMT and CMT-related properties. The principle of this method is to divide the CRM domain into subdomains with different horizontal sizes to mimic the GCM grid spacings with the assumptions that different spatial locations are uncorrelated and have the same statistics. First, we define clouds in convective updraft and downdraft regions using the following criteria (Liu et al. 2015): 1) vertical velocities ( $w$ )  $> 1 \text{ m s}^{-1}$ , and total hydrometeor mixing ratio ( $q_{\text{tot}}$ )  $> 1 \times 10^{-6} \text{ kg kg}^{-1}$ ; or 2)  $w > 2 \text{ m s}^{-1}$  for updrafts, and  $w < -1 \text{ m s}^{-1}$ , and  $q_{\text{tot}} > 1 \times 10^{-5} \text{ kg kg}^{-1}$  for downdrafts. Second, we divide the CRM domain,  $560 \times 560 \text{ km}^2$ , into subdomains with horizontal sizes of  $2 \times 2, 4 \times 4, 8 \times 8, 16 \times 16, 32 \times 32, 64 \times 64, 128 \times 128, 256 \times 256$ , and  $512 \times 512 \text{ km}^2$  by excluding the outermost 24-km area on each side. A subdomain can belong to one of seven different combinations of updraft, downdraft, and environment. These subdomain types include 1) updraft only; 2) downdraft only; 3) environment only; 4) updraft and environment; 5) downdraft and environment; 6) updraft, downdraft, and environment; and 7) updraft and downdraft. Our analysis considers only types 4, 5, and 6 because as far as CMT parameterization is concerned, types 1, 2, and 3 do not contribute to CMT. Although type 7 can have nonzero CMT because of differences in cloud properties between updrafts and downdrafts, it only appears when the subdomain size is smaller than 16 km, and its contribution to the total momentum transport (resolved momentum transport + CMT) is very small. Therefore, we exclude type 7 from the analysis as well.

The mathematical expressions for CRM-simulated CMT are provided below. Because MC3E-0523 is a nonlinear MCC system, the two horizontal components are in the zonal ( $x$ ) and meridional ( $y$ ) directions. For MC3E-0520 linear convective system (squall line), the two horizontal components are converted to the line-parallel and the line-normal components. They are also referred to as the  $x$  and  $y$  components, respectively. The CRM-simulated CMT in the  $x$  ( $\overline{\rho w' u'}$ ) and  $y$  directions ( $\overline{\rho w' v'}$ ) from the CRM simulations are defined as (Wu and Arakawa 2014; Zhang and Wu 2003)

$$\overline{\rho w' u'} = \rho \frac{1}{N} \sum_{i=1}^N (w_i - \bar{w})(u_i - \bar{u}), \quad (1a)$$

$$\overline{\rho w' v'} = \rho \frac{1}{N} \sum_{i=1}^N (w_i - \bar{w})(v_i - \bar{v}), \quad (1b)$$

where  $\rho$  is the air density and  $u_i, v_i,$  and  $w_i$  are the  $x, y,$  and  $z$  components of velocity ( $\text{m s}^{-1}$ ) at each CRM gridpoint  $i$  in a subdomain considered. Overbar and prime represent the mean over the subdomain and the deviation from it, respectively;  $N$  is the total number of grid points in the subdomain;  $\overline{\rho w' u'}$  and  $\overline{\rho w' v'}$  can be further partitioned into contributions from updrafts ( $U_{x_{\text{crm}}}, U_{y_{\text{crm}}}$ ) and downdrafts ( $D_{x_{\text{crm}}}, D_{y_{\text{crm}}}$ ) and environment ( $E_{x_{\text{crm}}}, E_{y_{\text{crm}}}$ ), with similar definitions to Eq. (1) except only those grid points satisfying their respective criteria are included, and the summation is over  $N_U, N_D,$  and  $N_E,$  respectively. Here,  $N_U, N_D,$  and  $N_E$  are the numbers of grid points in a subdomain containing updrafts, downdrafts, and environment, respectively. For a given grid spacing (e.g., 64 km), the number of such subdomains  $j$  within the CRM domain that meet conditions of 4, 5, and 6 is denoted by  $M$ . Then the ensemble-mean  $x$  ( $C_{x_{\text{crm}}}$ ) and  $y$  ( $C_{y_{\text{crm}}}$ ) components of CMT of are given by

$$C_{x_{\text{crm}}} = \frac{1}{M} \sum_{j=1}^M \rho(\overline{w'u'})_j, \quad (2a)$$

$$C_{y_{\text{crm}}} = \frac{1}{M} \sum_{j=1}^M \rho(\overline{w'v'})_j. \quad (2b)$$

In terms of parameterizations of CMT, the traditional top-hat approach ignored inhomogeneity within updrafts and downdrafts; thus, the subdomain-averaged updraft vertical velocity and  $x$ - and  $y$ -component horizontal velocities are calculated by

$$\hat{w}_U = \frac{1}{N_U} \left( \sum_{i=1}^{N_U} w_i \right), \quad \hat{u}_U = \frac{1}{N_U} \left( \sum_{i=1}^{N_U} u_i \right), \quad \text{and}$$

$$\hat{v}_U = \frac{1}{N_U} \left( \sum_{i=1}^{N_U} v_i \right),$$

respectively. The parameterized  $x$  component of CMT associated with updrafts, downdrafts, and environment (referred to as  $U_{x_{1\text{draft}}}, D_{x_{1\text{draft}}},$  and  $E_{x_{1\text{draft}}},$  respectively) in a subdomain using the one-draft (top hat) approach is given by

$$U_{x_{1\text{draft}}} = \sigma_U (\hat{w}_U - \bar{w}) (\hat{u}_U - \bar{u}), \quad (3a)$$

$$D_{x_{1\text{draft}}} = \sigma_D (\hat{w}_D - \bar{w}) (\hat{u}_D - \bar{u}), \quad (3b)$$

$$E_{x_{1\text{draft}}} = \sigma_E (\hat{w}_E - \bar{w}) (\hat{u}_E - \bar{u}), \quad (3c)$$

where subscripts  $U, D,$  and  $E$  denote the updraft, downdraft, and environment, respectively;  $\sigma_U, \sigma_D,$  and  $\sigma_E$  are the fractions of updraft, downdraft, and environmental areas, respectively. The parameterized  $y$  component of

updraft CMT ( $U_{y_{1\text{draft}}}$ ), downdraft CMT ( $D_{y_{1\text{draft}}}$ ), and environment CMT ( $E_{y_{1\text{draft}}}$ ) in a subdomain with the one-draft approach can be obtained with similar definitions to Eqs. (3a)–(3c) except that each  $u$  is replaced by  $v$ .

To account for the inhomogeneous structures of updrafts to better represent the convective transport of water vapor, Liu et al. (2015) adopted a three-updraft approach. By applying the three-updraft approach to the CMT,  $x$  and  $y$  components of updraft CMT (referred to as  $U_{x_{3\text{draft}}}, U_{y_{3\text{draft}}}$ ) in a subdomain can be calculated by

$$U_{x_{3\text{draft}}} = \sigma_{U1} (\hat{w}_{U1} - \bar{w}) (\hat{u}_{U1} - \bar{u}) + \sigma_{U2} (\hat{w}_{U2} - \bar{w}) (\hat{u}_{U2} - \bar{u}) + \sigma_{U3} (\hat{w}_{U3} - \bar{w}) (\hat{u}_{U3} - \bar{u}), \quad (4a)$$

$$U_{y_{3\text{draft}}} = \sigma_{U1} (\hat{w}_{U1} - \bar{w}) (\hat{v}_{U1} - \bar{v}) + \sigma_{U2} (\hat{w}_{U2} - \bar{w}) (\hat{v}_{U2} - \bar{v}) + \sigma_{U3} (\hat{w}_{U3} - \bar{w}) (\hat{v}_{U3} - \bar{v}), \quad (4b)$$

The three updrafts are defined as follows: 1)  $1 < w \leq 3 \text{ m s}^{-1}$ , and  $Q_{\text{tot}} > 10^{-6} \text{ kg kg}^{-1}$ , or  $2 < w \leq 3 \text{ m s}^{-1}$  for weak updrafts; 2)  $3 < w \leq 6 \text{ m s}^{-1}$  for medium-strength updrafts; and 3)  $w > 6 \text{ m s}^{-1}$  for strong updrafts (Arakawa and Wu 2013; Liu et al. 2015).

The vertical divergence of CMT is often called apparent momentum source  $X$ :

$$X_x = -\frac{\partial(\overline{\rho w' u'})}{\bar{\rho} \partial z}, \quad (5a)$$

$$X_y = -\frac{\partial(\overline{\rho w' v'})}{\bar{\rho} \partial z}. \quad (5b)$$

The apparent momentum source for updrafts can be approximated by (Shapiro and Stevens 1980; Wu and Yanai 1994; Zhang and Wu 2003)

$$X_{x_U} = M_U \frac{\partial \bar{u}}{\rho \partial z} + \delta (\hat{u}_U - \bar{u}) + \frac{1}{\rho} \sigma_U \left( \frac{\partial p}{\partial x} \right)_U, \quad (6a)$$

$$X_{y_U} = M_U \frac{\partial \bar{v}}{\rho \partial z} + \delta (\hat{v}_U - \bar{v}) + \frac{1}{\rho} \sigma_U \left( \frac{\partial p}{\partial y} \right)_U, \quad (6b)$$

where  $\delta$  is the air mass detrainment at the cloud boundaries and  $p$  is the perturbation pressure induced by convection. The apparent momentum source for downdrafts ( $X_{x_D}, X_{y_D}$ ) can be obtained with similar definitions to Eqs. (6a) and (6b) except that each subscript  $U$  is replaced by  $D$ . The first term on the right-hand side of Eqs. (6a) and (6b) is the product of the updraft mass flux and the vertical mean wind shear, which can be interpreted as the vertical advection of mean horizontal momentum by compensating subsidence; the second term represents the

effect of horizontal momentum that is detrained from updrafts into environment; the last term is the effect of the CIPG force on environment.

To further explore the scale dependency of CIPG, we adopt the approximated budget equation for CIPG from Zhang and Wu (2003):

$$\begin{aligned} \nabla^2(\nabla p) = & \nabla \left[ -2\rho \left( \frac{\partial w}{\partial x} \frac{\partial \bar{u}}{\partial z} + \frac{\partial w}{\partial y} \frac{\partial \bar{v}}{\partial z} \right) \right] + \nabla \left[ -2\rho \left( \frac{\partial w}{\partial x} \frac{\partial u'}{\partial z} + \frac{\partial w}{\partial y} \frac{\partial v'}{\partial z} \right) \right] \\ & + \nabla \left\{ -\rho \left[ \left( \frac{\partial u}{\partial x} \right)^2 + \left( \frac{\partial v}{\partial y} \right)^2 + \left( \frac{\partial w}{\partial z} \right)^2 \right] \right\} + \nabla \left[ w^2 \rho \frac{\partial}{\partial z} \left( \frac{1}{\rho} \frac{\partial \rho}{\partial z} \right) \right] + \nabla \left( \frac{\partial \rho B}{\partial z} \right). \end{aligned} \quad (7)$$

Here,  $\nabla^2$  is the 3D Laplacian operator ( $\partial^2/\partial x^2 + \partial^2/\partial y^2 + \partial^2/\partial z^2$ ). The first four terms on the right-hand side represent the dynamic contributions to the Laplacian of CIPG and are referred to as the linear-shear forcing, nonlinear-shear forcing, the divergence forcing, and density stratification forcing, respectively (Rotunno and Klemp 1982; Zhang and Wu 2003). The last term on the right-hand side is the buoyancy forcing of the cloud air. To examine their relative contributions to the Laplacian of CIPG, the first four terms on the right-hand side and the Laplacian of CIPG on the left-hand side are directly calculated from CRM data, while the buoyancy term on the right-hand side is estimated as the residual.

The GKI97 scheme includes only the linear-shear forcing for parameterizing CIPG and can be expressed as

$$\frac{\sigma_U}{\rho} \left( \frac{\partial p}{\partial x} \right)_U = -C_{U_x} M_U \frac{\partial \bar{u}}{\partial z}, \quad (8a)$$

$$\frac{\sigma_D}{\rho} \left( \frac{\partial p}{\partial x} \right)_D = -C_{D_x} M_D \frac{\partial \bar{u}}{\partial z}, \quad (8b)$$

$$\frac{\sigma_U}{\rho} \left( \frac{\partial p}{\partial y} \right)_U = -C_{U_y} M_U \frac{\partial \bar{v}}{\partial z}, \quad (8c)$$

$$\frac{\sigma_D}{\rho} \left( \frac{\partial p}{\partial y} \right)_D = -C_{D_y} M_D \frac{\partial \bar{v}}{\partial z}, \quad (8d)$$

where  $C_{U_x}$ ,  $C_{D_x}$ ,  $C_{U_y}$ , and  $C_{D_y}$  are coefficients. In the current GKI97 CMT scheme,  $C_{U_x}$ ,  $C_{D_x}$ ,  $C_{U_y}$ , and  $C_{D_y}$  are set to the same value ( $C$ ). In the next section, we examine the relative contributions from each forcing to the Laplacian of CIPG at different model grid spacings. This can provide evidence for justifying the approximation used in the GKI97 scheme for all grid spacings.

To further quantify the performance of the GKI97 scheme for parameterizing CIPG at different grid spacings, we conduct a linear regression analysis for Eqs. (8a)–(8d) using the product of mass flux and vertical mean wind shear as the predictor variable and CRM-derived CIPG as the response variable. The adjusted coefficient of determination ( $R_{\text{adj}}^2$ ) obtained from linear regression analysis indicates how well the CRM-derived

CIPG variation can be explained by the product of mass flux and vertical mean wind shear (the GKI97 scheme). The formula for  $R_{\text{adj}}^2$  is as follows:

$$\begin{aligned} R_{\text{adj}}^2 &= 1 - \left( \frac{\text{SS}_{\text{resid}}}{\text{SS}_{\text{total}}} \right) \times \left( \frac{n-1}{n-d-1} \right) \\ &= 1 - R^2 \left( \frac{n-1}{n-d-1} \right), \end{aligned} \quad (9)$$

where  $R^2$  is the coefficient of determination, which is the ratio of  $\text{SS}_{\text{resid}}$  (the sum of the squared residuals from the regression) and  $\text{SS}_{\text{total}}$  (the sum of the squared differences from the mean of the dependent variable, or the total sum of squares),  $d$  is the total number of predictor variables in the regression equation, and  $n$  is the sample size. The larger  $R_{\text{adj}}^2$  is, the more variability in the response variable is explained by the predictor variables. In addition to  $R_{\text{adj}}^2$ , the Pearson correlation coefficient (CC) is also calculated to examine the linear dependence between the CRM-derived CIPG and the product of mass flux and vertical mean wind shear [Eq. (8)].

The statistical significance for the regression analysis and CC is examined using the  $F$  test, and they are considered statistically significant when satisfying the threshold to reject the null hypothesis at 95% level. The statistical significance test can help discard unrealistic results that are obtained when the sample size is too small, especially when the grid spacing is large (128–512 km).

Because the cloud mass flux is an important parameter for parameterizing the CMT in the GKI97 scheme, convective updraft and downdraft mass fluxes are also computed to explore their scale dependency. The updraft mass flux and downdraft mass flux are computed by

$$M_U = \rho \sigma_U (\hat{w}_U - \hat{w}_E), \quad (10a)$$

$$M_D = \rho \sigma_D (\hat{w}_D - \hat{w}_E). \quad (10b)$$

Note that mean vertical velocity of environmental air  $\hat{w}_E$ , instead of grid-mean  $\bar{w}$ , is included.

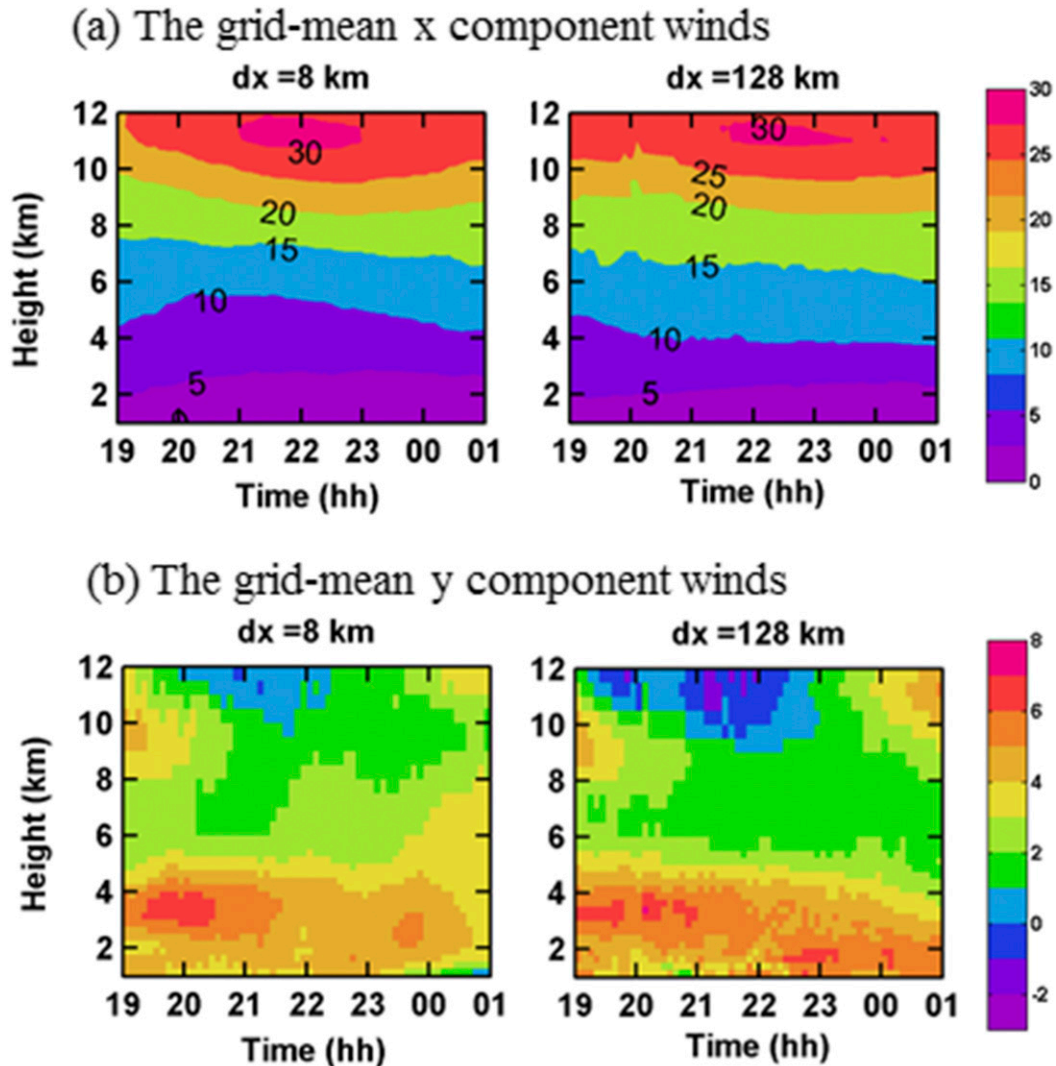


FIG. 1. Time–height cross sections of grid-mean (a)  $x$ -component winds ( $\bar{u}$ ,  $\text{m s}^{-1}$ ) and (b)  $y$ -component winds ( $\bar{v}$ ,  $\text{m s}^{-1}$ ) averaged over the ensemble domains at (left)  $dx = 8$  and (right)  $dx = 128$  km for MC3E-0523. Time period is from 1930 UTC 23 May to 0130 UTC 24 May. Please refer to Fig. S1 for the results of all different grid spacings.

#### 4. Results

##### a. Scale dependency of CRM-simulated mass flux and CMT

Figure 1 shows the time–height cross sections of the ensemble-mean grid-mean winds ( $\bar{u}$  and  $\bar{v}$ ) for 8- and 128-km grid spacings from the MC3E-0523 case [see Fig. S1 in the supplemental information (SI) for all different grid spacings]; “ensemble mean” [see Eq. (2) for its definition] will be omitted for brevity. The analysis time period is from 1930 UTC 23 May to 0130 UTC 24 May, when the MCC evolves from the initial developing, intensifying, to mature stages. It shows that the grid-mean  $x$  component of winds ( $\bar{u}$ ) are westerly

throughout the troposphere with the maximum wind speeds in the upper troposphere during the entire period (Fig. 1a). The grid-mean  $y$  component of winds ( $\bar{v}$ ) are southerly in most of the troposphere except for 2100–2300 UTC above 10-km height, and the maximum  $\bar{v}$  occurs in the lower troposphere (Fig. 1b). In general, the time–height cross-sections of  $\bar{u}$  and  $\bar{v}$  are very similar for different grid spacings except weaker westerly winds and stronger northerly winds above 10-km altitude for larger grid spacings. This indicates a weak scale dependency for grid-mean wind components. The grid-mean  $x$  component of winds ( $\bar{u}$ ) from MC3E-0520 shows results similar to MCE-0523 (Fig. 2a), demonstrating a weak scale dependency as well. However, the grid-mean  $y$

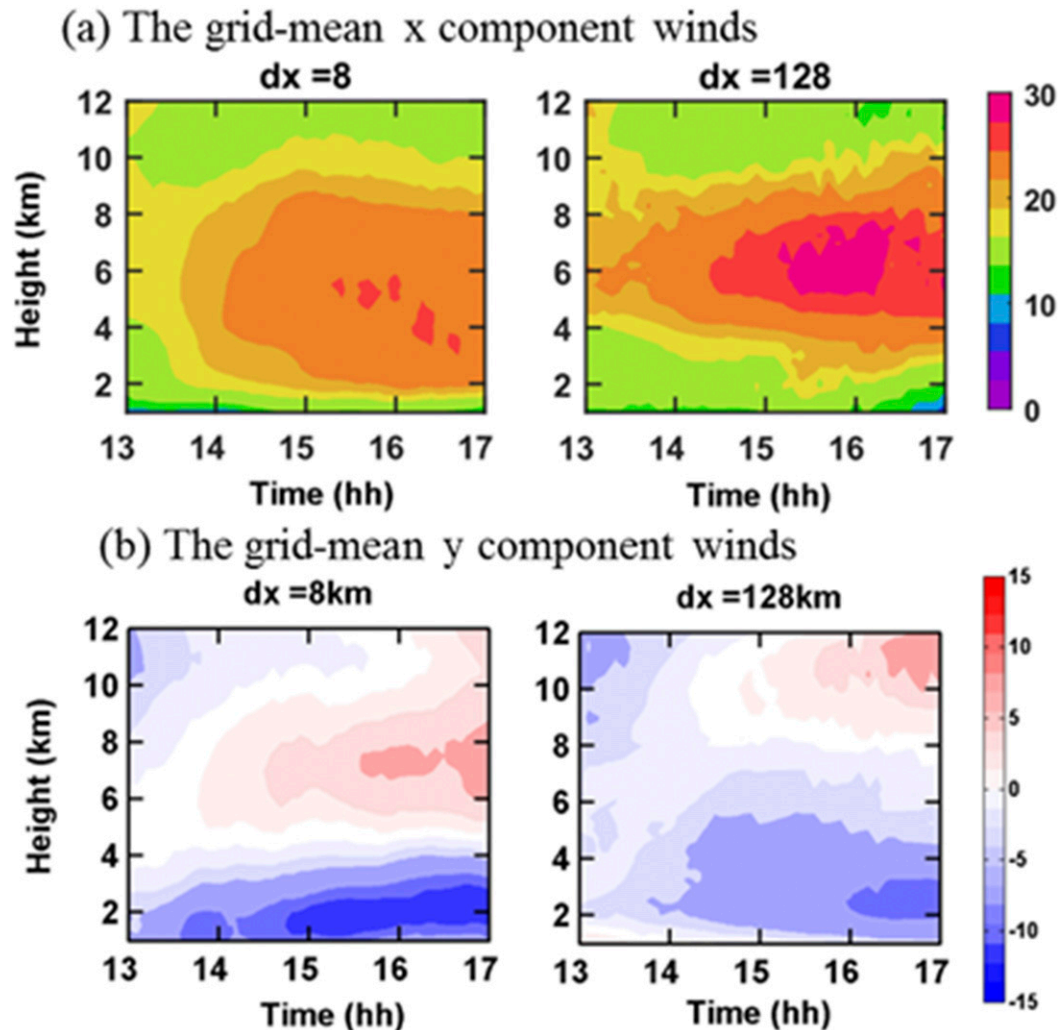


FIG. 2. As in Fig. 1, but from MC3E-0520. Time period is from 1300 to 1700 UTC 20 May. Please refer to Fig. S2 for the results of all different grid spacings.

component of winds ( $\bar{v}$ ) from MC3E-0520 exhibits distinct differences between small and large grid spacings (Fig. 2b and Fig. S2), as indicated by the gradual decrease of vertical gradient as the grid spacing increases from  $dx = 4$ –16 to  $dx = 32$ –512 km.

To understand what contributes to the different vertical structures of  $\bar{v}$  between the small ( $dx = 4$ –16 km) and large ( $dx = 32$ –512 km) grid spacings from MC3E-0520, snapshots of the horizontal distribution of  $\bar{v}$  at 6.0-km altitude for  $dx = 8$  and 128 km are shown in Fig. 3. In Figs. 3a and 3b, only the subdomains that meet conditions 4, 5, and 6 for  $dx = 8$  and 128 km are plotted to represent the small and large grid spacings, respectively. The selected subdomains for  $dx = 128$  km occupy much larger regions than those for  $dx = 8$  km. The latter are closer to where the squall line is located

(Fig. 3c). In addition, for  $dx = 128$  km, the majority of the subdomains contain negative  $\bar{v}$ , resulting in negative ensemble-mean  $\bar{v}$ . However, for  $dx = 8$  km, the majority of the subdomains have positive  $\bar{v}$ , producing positive ensemble-mean  $\bar{v}$ . This explains the different upper-level winds between large and small grid spacings, and where the scale dependency of  $\bar{v}$  comes from.

The updraft and downdraft mass fluxes show considerable differences among different grid spacings of MC3E-0523 (Fig. 4 and Fig. S3 in SI). The updraft mass fluxes decrease monotonically as subdomain size–grid spacing ( $dx$ ) increases and peak from the initial developing stage at small grid spacings to the mature stage at very large grid spacings, while downdraft mass fluxes peak at  $dx = 8$  or 16 km and then decrease as  $dx$  increases (Fig. S3). Note that subdomain size and grid

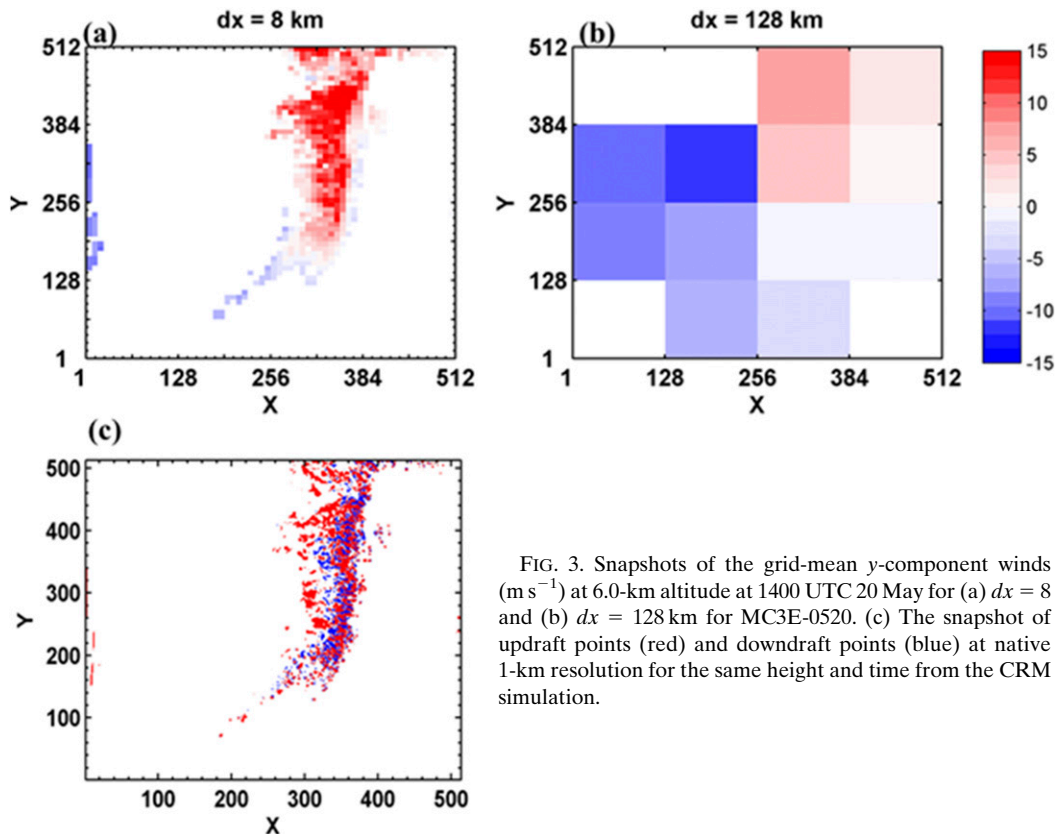


FIG. 3. Snapshots of the grid-mean  $y$ -component winds ( $\text{m s}^{-1}$ ) at 6.0-km altitude at 1400 UTC 20 May for (a)  $dx = 8$  and (b)  $dx = 128$  km for MC3E-0520. (c) The snapshot of updraft points (red) and downdraft points (blue) at native 1-km resolution for the same height and time from the CRM simulation.

spacing are used interchangeably throughout the rest of the paper. In addition, downdraft mass fluxes peak near 4-km altitude where the freezing level is located and at the mature stage for all the grid spacings (Zhang and Wu 2003). The different temporal evolution between updraft mass fluxes and downdraft mass fluxes is because strong downdrafts do not develop coincidentally with updrafts; thus, downdraft intensity is weaker at the early stage of development and becomes stronger at the mature stage as strong precipitation forms. The MC3E-0520 squall line shows similar results to MCE-0523 (figures not shown), indicating that both updraft and downdraft mass fluxes have strong scale dependency.

As expected, the time–height cross sections of CMT show even larger differences among different grid spacings relative to those of either updraft or downdraft mass fluxes because CMT is the product of fluctuations of both horizontal and vertical wind components (Fig. 5 and Fig. S4). Here, we only show results from MC3E-0523 as an example. Figure S4 shows that for all grid spacings the  $x$  component of updraft CMT is negative throughout the troposphere during 1930 UTC 23 May–0130 UTC 24 May. This indicates that there is downward momentum transport in westerlies.

For small grid spacings, the updraft CMT peaks from the initial developing stage compared to the mature stage for the very coarse grid spacings, which is largely similar to updraft mass flux. For example, at  $dx = 4$  km (Fig. S4a), the absolute maximum CMT occurs in the first few hours of development and then decreases significantly with time. At  $dx > 64$  km, the CMT magnitude is small at the first 2 h of development and increases afterward as in updraft mass flux (Fig. 4a). Also, as the grid spacing gets coarser, the CMT magnitude increases in the upper troposphere ( $>10$ -km altitude), perhaps because of better-organized flows, for example, the anvil outflows.

Opposite to its  $x$ -component counterpart, the  $y$  component of updraft CMT is mostly positive except for  $dx < 32$  km at the first hour and for  $dx > 32$  km below the 2-km altitude (Fig. 6a and Fig. S5a), indicating mostly upward momentum transport in southerlies. Further, the magnitude increases with the grid spacing more significantly than that of its  $x$ -component counterpart.

Both  $x$  and  $y$  components of downdraft CMT show more significant changes as the grid spacing increases than their updraft counterparts (Figs. 5b, 6b and Figs. S4b, S5b). For the  $x$  component of downdraft CMT (Fig. 5b and Fig. S4b), as the grid spacing increases, it evolves from mostly negative at  $dx < 16$  km to mostly

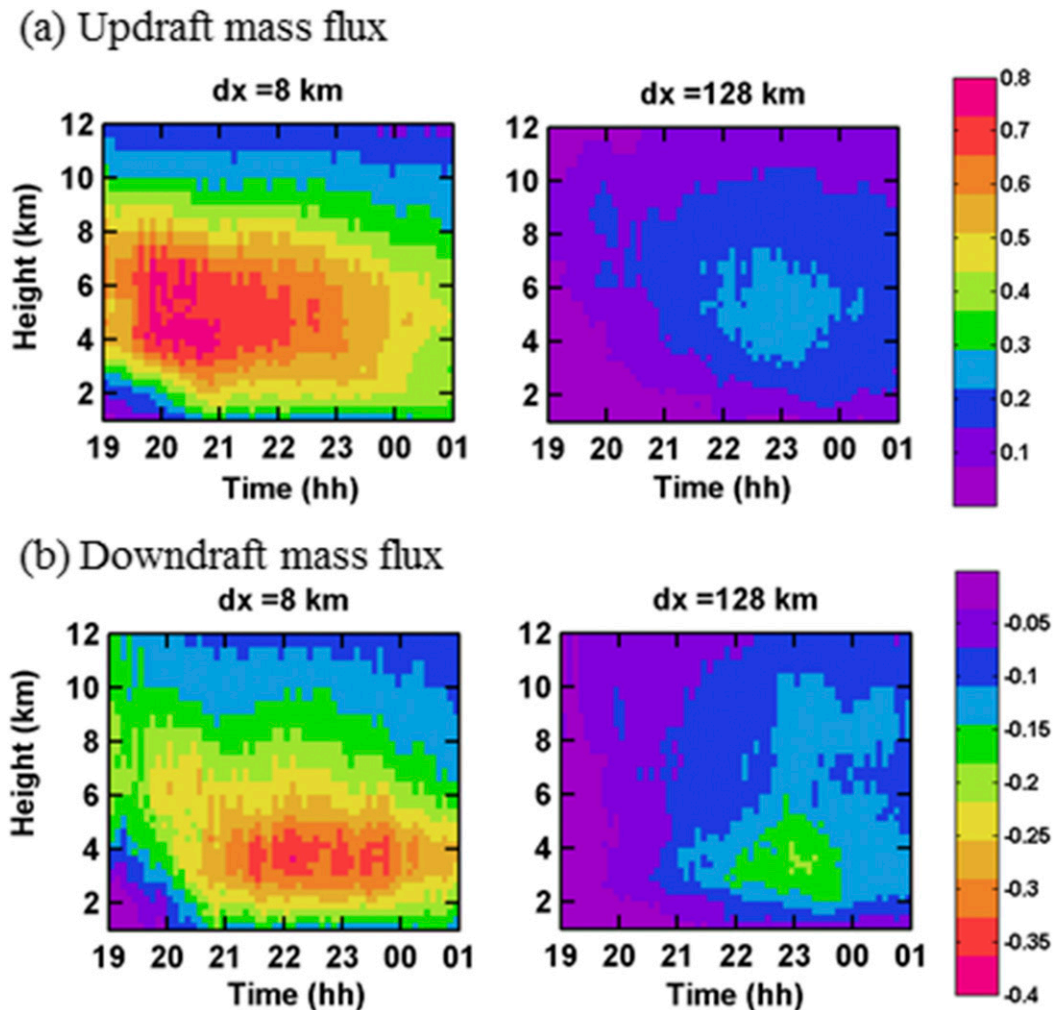


FIG. 4. As in Fig. 1, but for ensemble-mean mass flux ( $\text{kg m}^{-2} \text{s}^{-1}$ ) in (a) convective updrafts and (b) downdrafts. Please refer to Fig. S3 for the results of all different grid spacings.

positive at and above  $dx > 64$  km. As for the  $y$  component (Fig. 6b and Fig. S5b), it evolves from mostly positive (except at low levels after 0000 UTC 24 May) for  $dx = 4$ – $32$  km to changing signs in the vertical for  $dx = 64$ – $512$  km (i.e., negative CMT at the 4–8-km altitude but positive CMTs below 4- and above 8-km altitudes). As in the mass fluxes (Fig. 4), downdraft CMTs peak in the lower troposphere while updraft CMTs are significant over a much larger extent of the troposphere.

In summary, the grid-unresolved properties, such as mass flux and CMT, have a much stronger scale dependency than grid-resolved properties, such as the grid-mean winds. Both CMT and mass fluxes have strong scale dependencies with stronger CMTs, but their temporal and vertical changes can be mostly explained by those of their corresponding mass fluxes. The magnitudes of updraft CMT depend on the organized

flows that are stronger for the mature stage than for the initial stage of convective systems.

#### b. Relationships between CMT and wind shear

Previous studies have shown that for linear MCS such as squall line, CMT may be upgradient in the line-normal ( $y$ ) direction and downgradient in the line-parallel ( $x$ ) direction. On the other hand, CMT is generally downgradient for nonlinear MCS (Asai 1970; LeMone 1983; LeMone and Jorgensen 1991). To investigate whether the simulation reproduces the prevalent CMT characteristics and how the simulated CMT characteristics vary with grid spacings, the CMT profiles (updraft, downdraft, and total) overlaid with the grid-mean vertical wind shear profile are shown in Fig. 7. The grid-mean vertical- $x$ -component wind shear is calculated by

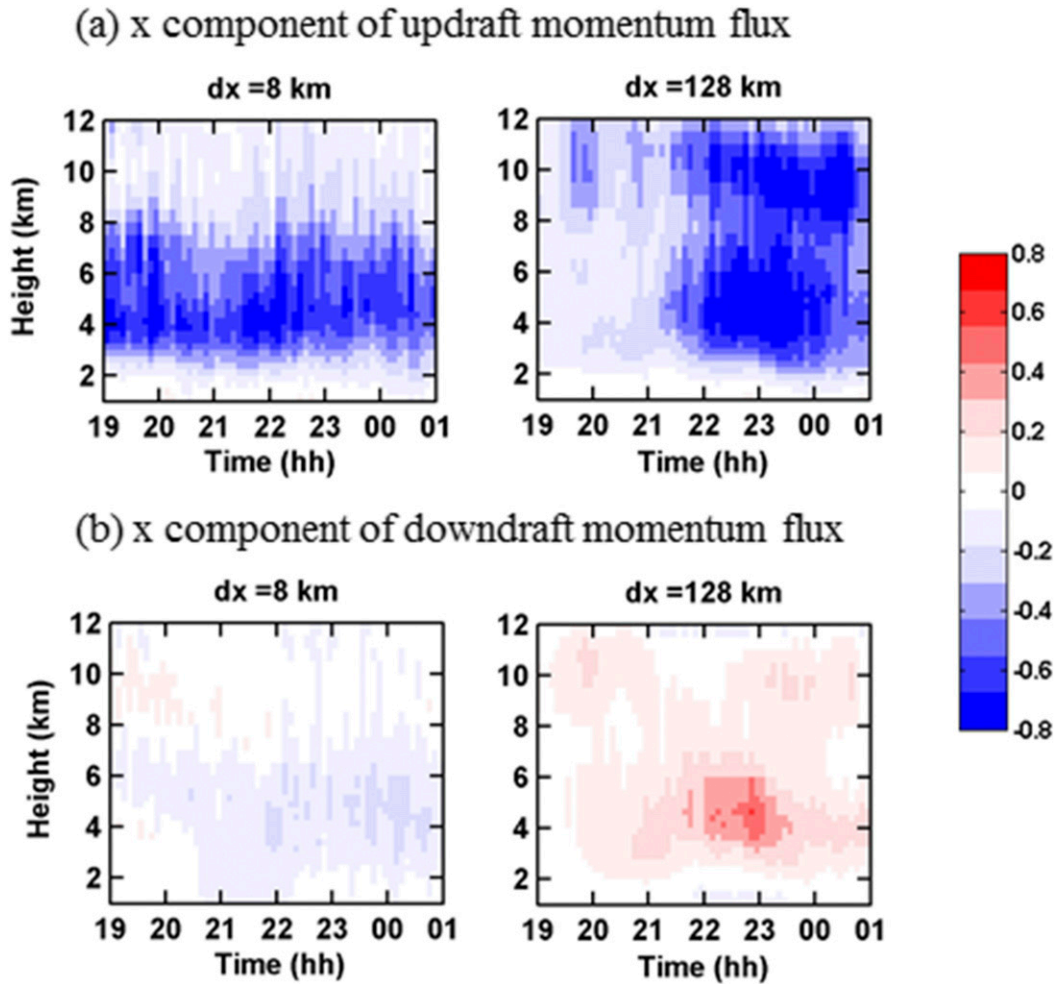


FIG. 5. As in Fig. 4, but for the x component of ensemble-mean vertical momentum flux ( $\text{kg m}^{-1} \text{s}^{-2}$ ). Please refer to Fig. S4 for the results of all different grid spacings.

$$(\bar{u}_{k+1} - \bar{u}_k) / |Z_{k+1} - Z_k|, \quad (11)$$

where  $Z_k$  is the altitude of vertical level  $k$ . Because of the small differences in the results (discussed below) within either the large grid spacings or the small grid spacings group, we select results at  $dx = 128$  and  $8 \text{ km}$  to represent the GCM scale and gray-zone scale, respectively, for brevity.

For MC3E-0523 (nonlinear MCS), comparing the  $x$  and  $y$  components of updraft and total CMTs with the grid-mean vertical wind shear shows that updraft and total CMT and vertical wind shear are generally opposite in sign at both large and small grid spacings, indicating that both the  $x$  and  $y$  components of total and updraft CMTs are downgradient with respect to vertical wind shear (Fig. 7a). An exception occurs around the 7-km altitude for the  $y$  component of  $dx = 128 \text{ km}$ . A similar downgradient transport can also be

seen from the  $x$  and  $y$  components of downdraft CMT at  $dx = 8 \text{ km}$ , but it is upgradient at  $dx = 128 \text{ km}$ . This suggests that downdraft CMT is very sensitive to grid spacing and can have different transport directions for small and large grid spacings, which is consistent with what is shown in Figs. 5b and 6b, even though the downdraft CMT is much smaller than its updraft counterpart, especially in the upper troposphere.

For MC3E-0520 (linear MCS), the  $x$  components of updraft, downdraft, and total CMTs for  $dx = 8$  and  $128 \text{ km}$  are generally opposite in sign to the grid-mean wind shear (except for downdraft CMT above the 8-km altitude at  $dx = 128 \text{ km}$  with small magnitudes), indicating downgradient transport (Fig. 7b). As for the  $y$  component, the relationship between CMTs and grid-mean wind shear exhibits some differences between  $dx = 8$  and  $dx = 128 \text{ km}$ . At  $dx = 128 \text{ km}$ , the grid-mean wind shear above 2-km heights as well as updraft and total CMTs at all levels

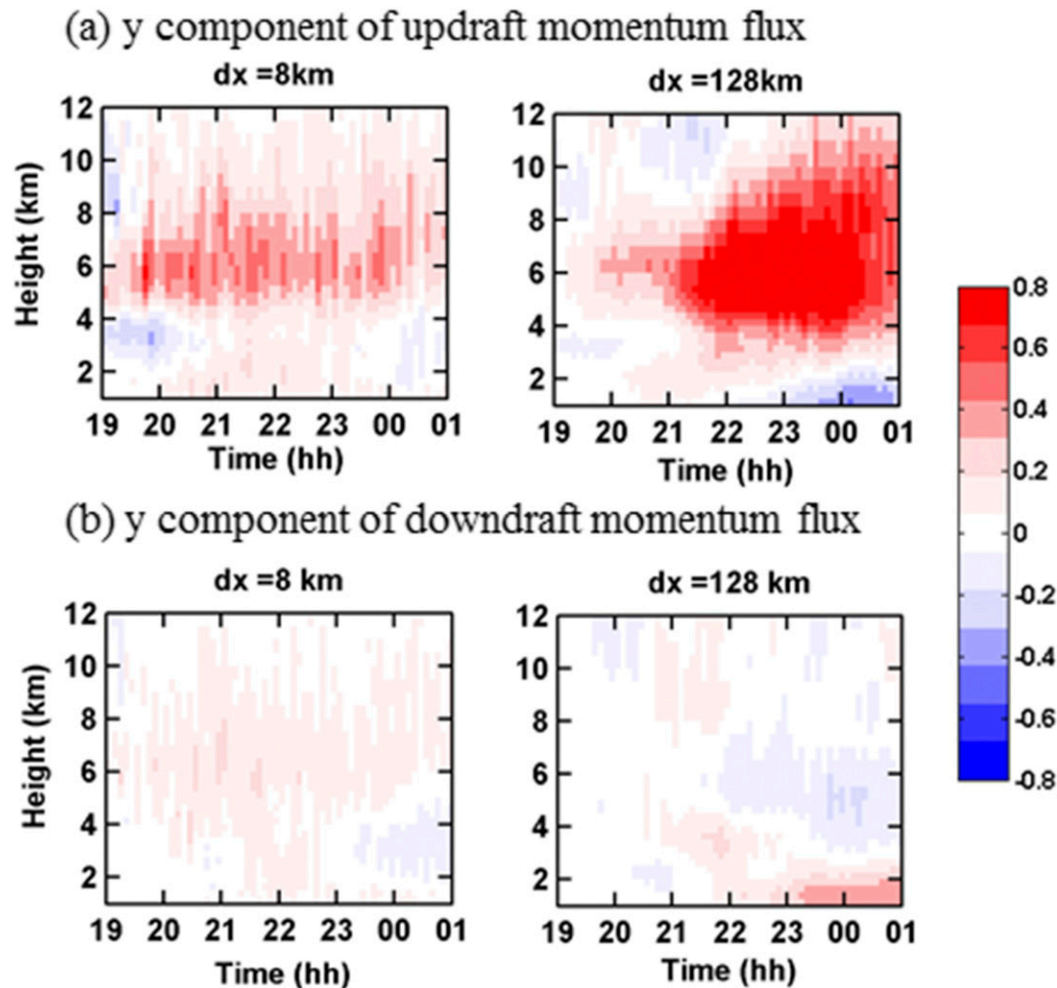


FIG. 6. As in Fig. 5, but for the y component. Please refer to Fig. S5 for the results of all different grid spacings.

are positive, indicating an upgradient momentum transport, while the downdraft momentum transport is downgradient at all levels (also for  $dx = 8$  km). At  $dx = 8$  km, the updraft and total CMTs are mostly positive at all levels, while the grid-mean vertical wind shears are negative above 7- and below 2-km height, and are positive between 2- and 7-km height, which suggests an upgradient transport below 7-km height and downgradient transport above 7 km. The difference in the grid-mean wind shear can be deduced from the vertical profiles of grid-mean wind shear in the y direction between  $dx = 8$  and  $dx = 128$  km (Fig. 2).

Based on the results shown above, for the nonlinear MCS (MC3E-0523), the downgradient transports for updrafts and total CMTs generally do not change with grid spacings and are consistent with previous studies. In contrast, downdraft CMT has downgradient transport at small grid spacings but becomes upgradient at large grid spacings. The upgradient CMT for downdrafts

is consistent with Zhang and Wu (2003). As for the linear MCS (MC3E-0520), the downgradient transport in the line-parallel direction and upgradient transport in the line-normal direction suggested by previous studies are reproduced for updraft and total CMTs at both the small and large grid spacings except for the line-normal component above 7-km height at small grid spacings. The downdraft CMT, on the other hand, is always downgradient regardless of the grid spacings for both line-parallel and line-normal components. These results suggest that prevalent CMT characteristics based upon field campaigns and model calculation for spatial scales typical of current GCM resolution is applicable to updrafts but not downdrafts across a wide range of grid spacings examined in this study.

To explain why the characteristics of updraft CMT are different between the y and x components as well as between the small and large grid spacings for the y

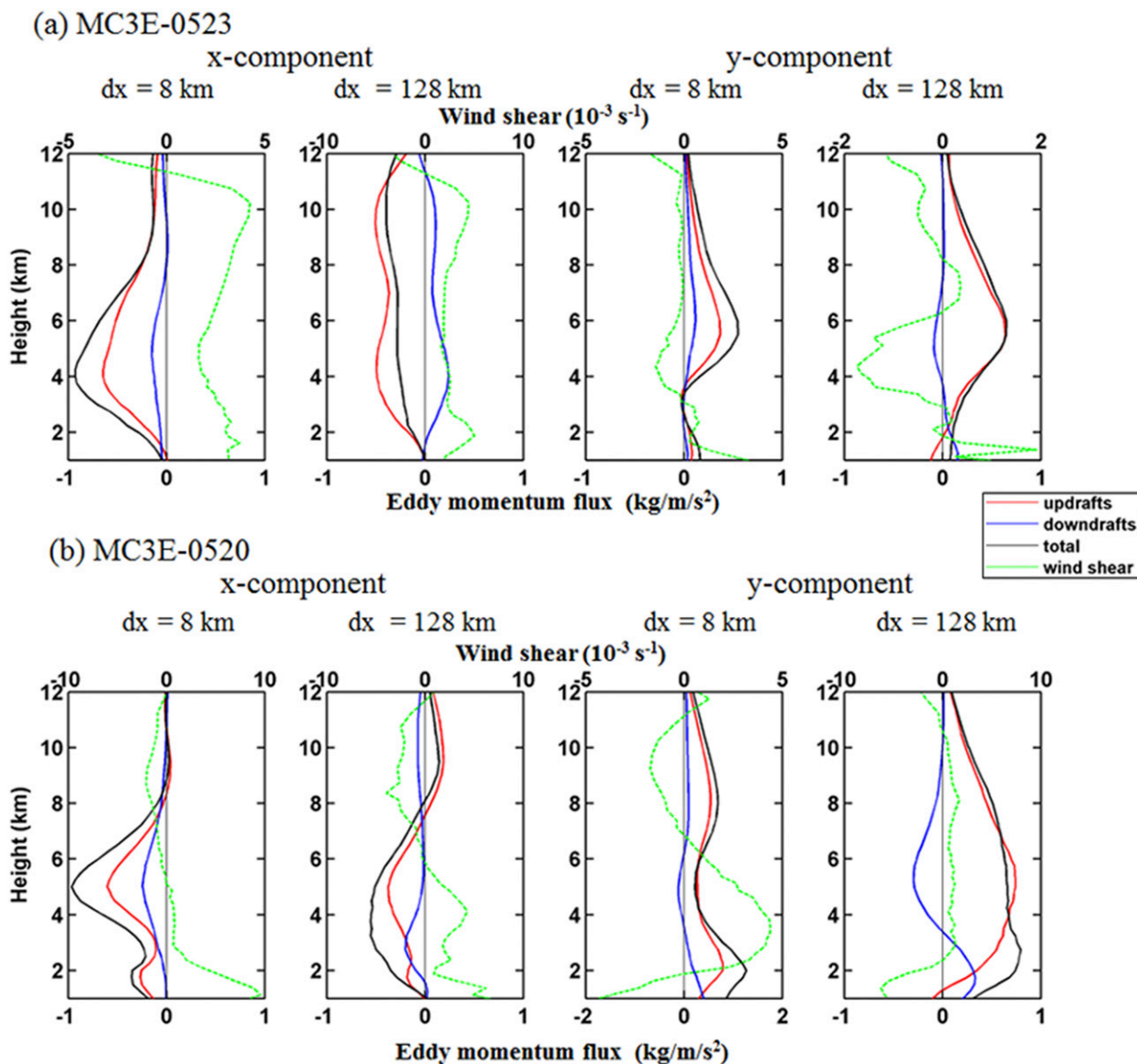


FIG. 7. Vertical profiles of the ensemble mean of the convective momentum fluxes and grid-mean vertical wind shear for (a) MCE3-0523 and (b) MC3E-0520. The red, blue, and black solid lines denote updrafts, downdrafts, and total convective momentum fluxes, respectively, with the scale shown on the bottom horizontal axis. The green dotted line is for grid-mean vertical wind shear with the scale shown on the top horizontal axis. (left two columns) The  $x$  component and (right two columns)  $y$  component at  $dx = 8$  and 128 km.

component, snapshots of updraft CMT and updraft PGF in the line-parallel and line-normal directions are shown in Figs. 8–11. These snapshots are similar to those shown in Figs. 3a and 3b for the  $y$ -component winds. Figures 8 and 9 show the  $x$  component of updraft CMT and PGF in convective updrafts at 4.5- and 9-km altitudes, respectively, at 1500 UTC 20 May when the squall line is at the intensifying stage. At 4.5-km altitude (Fig. 8), the majority of the  $x$  component of updraft CMTs is negative with exception for one subdomain at  $dx = 128$  km

and a few subdomains for  $dx = 8$  km. The negative  $x$  component of updraft CMT indicates that the air feeding the updrafts carries negative perturbation wind ( $u'$ ). Because the  $x$  component of updraft PGFs is mostly positive, the updraft PGF is opposite to the direction of the perturbation wind ( $u'$ ) in updrafts, decelerating the perturbation wind when air moves upward inside updrafts. As a result, the CMT at both large and small grid spacings is downgradient. A similar relation between the updraft CMT and PGF can also be

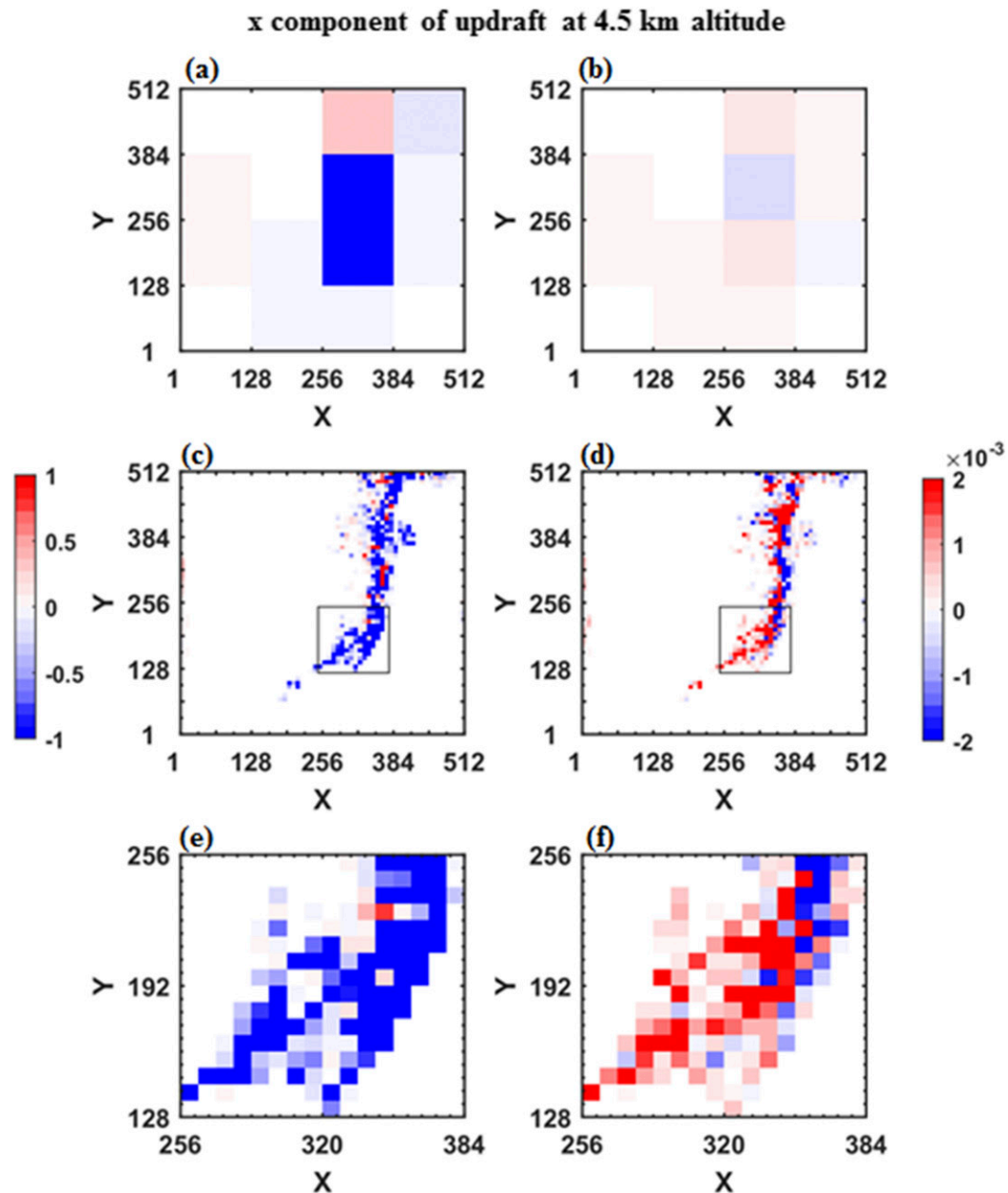


FIG. 8. The horizontal cross section of the  $x$  component of (a),(c),(e) updraft convective momentum flux ( $\text{kg m}^{-1} \text{s}^{-2}$ ) and (b),(d),(f) updraft pressure gradient force ( $\text{m s}^{-2}$ ) for (a),(b)  $dx = 128$  and (c)–(f)  $dx = 8$  km at 4.5-km altitudes at 1400 UTC 20 May; (e) and (f) are the closer look at the results within the black square in (c) and (d), respectively.

seen at 9.0-km altitude except the updraft CMT is mainly positive while the updraft PGF is negative (Fig. 9).

Figures 10 and 11 are the same as Figs. 8 and 9 except for the line-normal component at 4.5- and 7.5-km altitudes. Note that 7.5-km instead of 9-km altitude is chosen because the  $y$  component of maximum updraft CMT is located at a lower altitude. At 4.5-km altitude

(Fig. 10), the majority of line-normal updraft CMT at both small and large grid spacings is positive, indicating that the air entering convective updrafts carries positive perturbation wind ( $v'$ ). The positive  $y$  component of updraft PGF is in the same direction as the perturbation wind ( $v'$ ) in the updrafts, accelerating the perturbation wind, resulting in upgradient CMT for both small and large grid spacings.

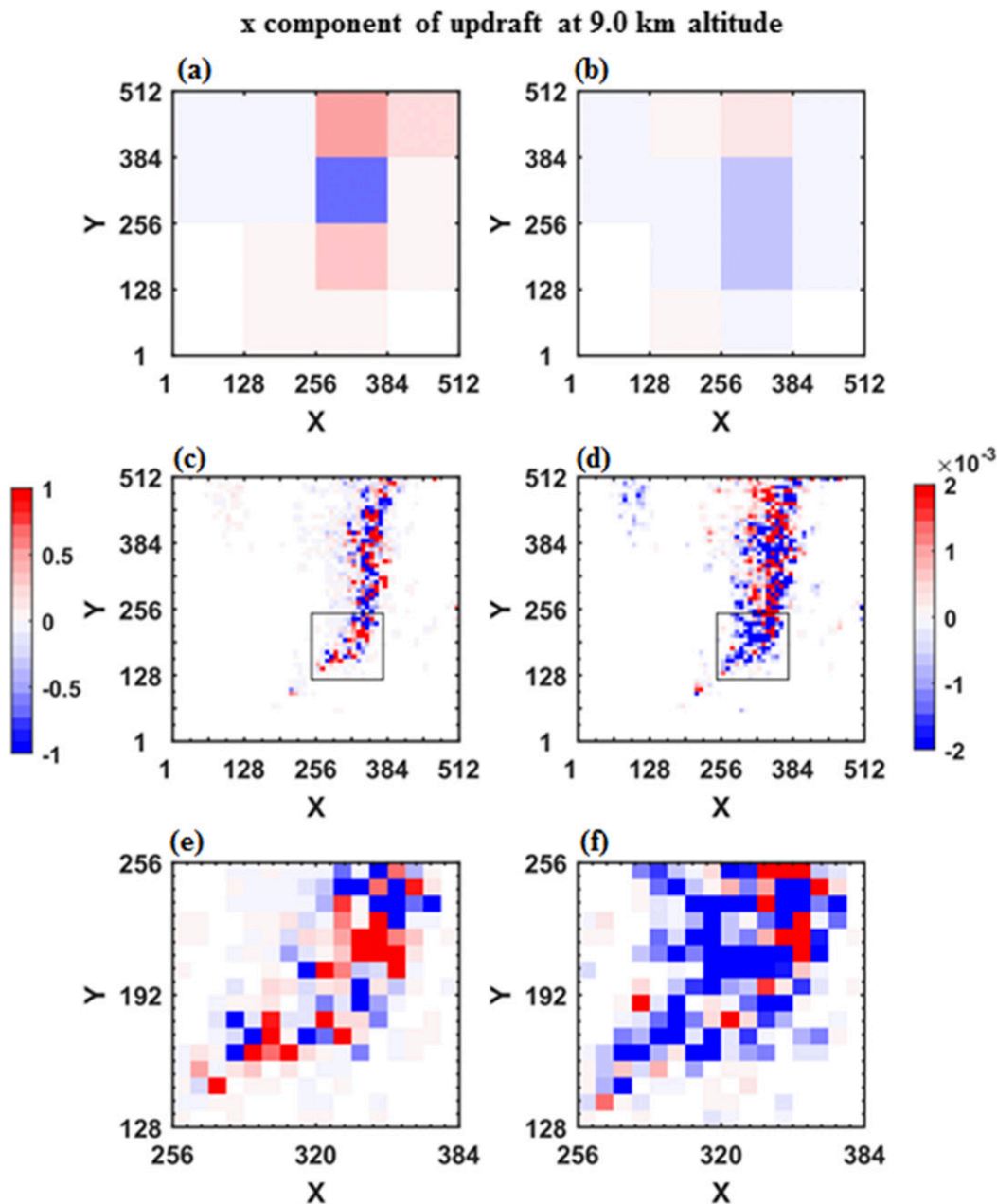


FIG. 9. As in Fig. 8, but for the x component at 9-km altitude.

For large grid spacings at 7.5-km altitude, the y component of updraft CMT and updraft PGF are mostly positive, indicating that the updraft PGF accelerates the perturbation wind in the updrafts, resulting in upgradient CMT. However, for small grid spacing, the majority of updraft CMT remains positive, but a large area of updraft PGF where the positive updraft CMT is located becomes negative, leading to decelerating the perturbation wind and downgradient CMT. This explains why the y component of updraft CMT becomes

downgradient transport above 7 km for small grid spacings. The results here suggest that the effect of PGF on updraft CMT characteristics is consistent across all grid spacings. The aforementioned relationship between the updraft CMT direction and PGF has also been used to explain the different CMT characteristics in the westerly and easterly wind regimes in Zhang and Wu (2003).

To examine whether the CMT characteristics are also controlled by PGF in convective downdrafts,

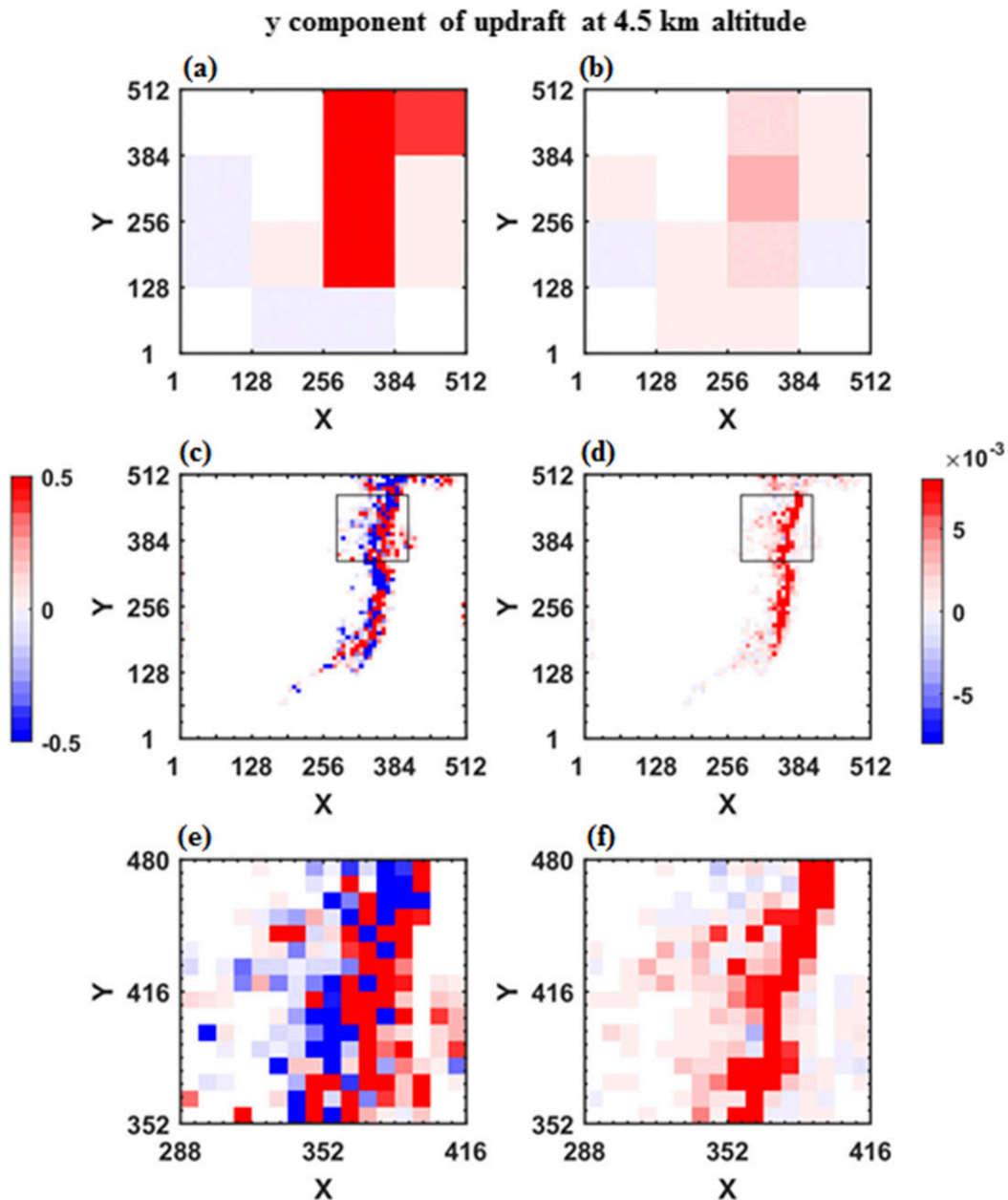


FIG. 10. As in Fig. 8, but for the y component at 4.5-km altitude.

snapshots of downdraft CMT and PGF at 4.5-km altitudes in the  $x$  and  $y$  directions are also shown in Figs. S6 and S7 in SI, respectively. Unlike the relation between the updraft CMT and PGF, the downdraft CMT and PGF do not have systematic relation for both the  $y$  and  $x$  components. The different signs of downdraft CMT when transitioning from the large to small grid spacings cannot be explained by the downdraft PGF as in updraft CMT. This may be expected because downdraft is largely contributed by

precipitation, which could make the sign of downdraft CMT more influenced by the size of grid spacing via cloud microphysical processes.

### c. Scale dependency of apparent momentum source and CIPG

Apparent momentum source is defined as the vertical gradient of CMT [Eq. (5)]. To examine the importance of CIPG to apparent momentum source, vertical profiles of the individual terms in Eq. (6) and apparent

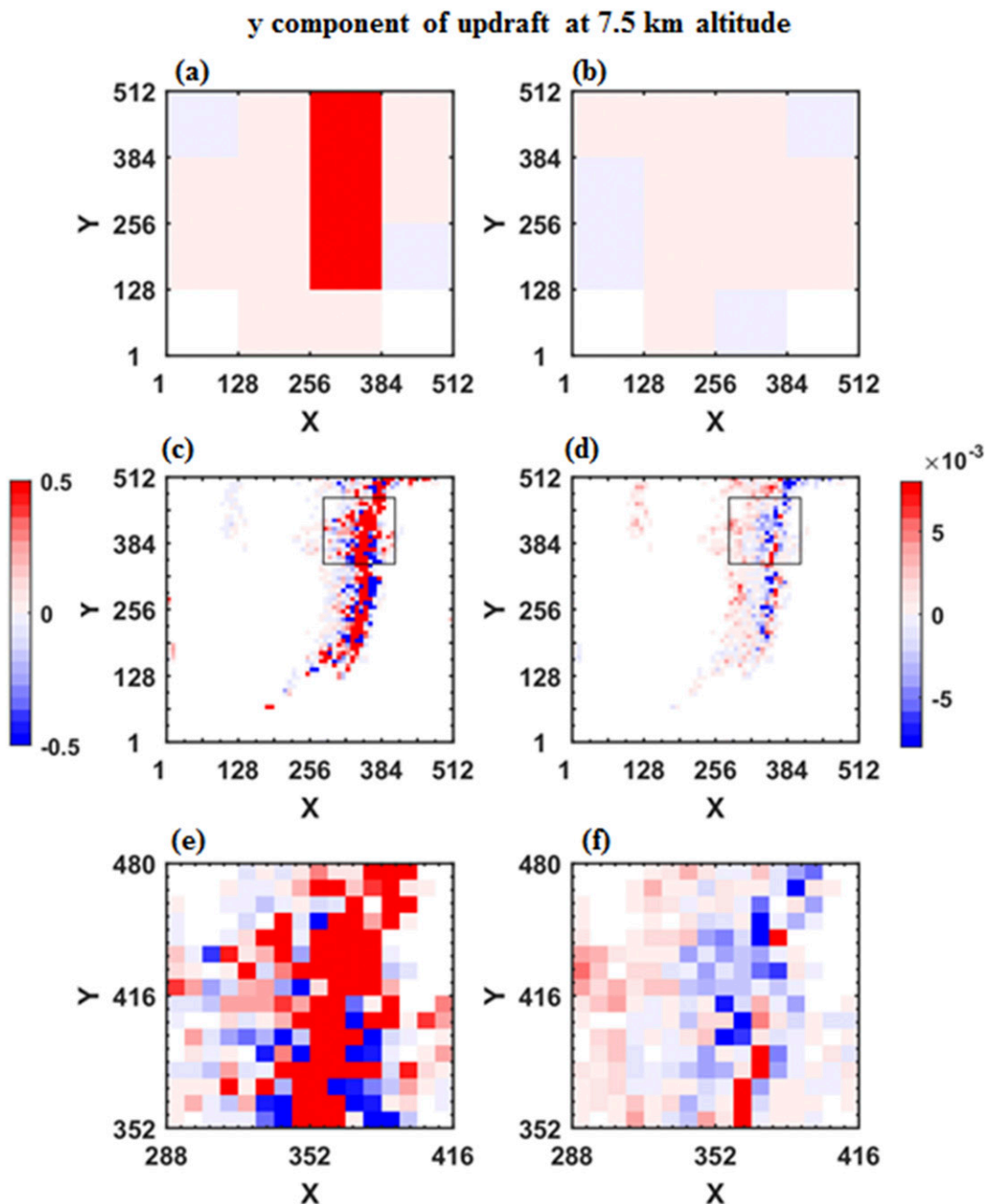


FIG. 11. As in Fig. 8, but for the y component at 7.5-km altitude.

momentum source across all the grid scales are compared in Fig. 12. Note that the detrainment term is estimated as the residual because the other three terms can be directly calculated from CRM data.

As shown in Fig. 12a, apparent momentum source varies significantly with height and grid spacing for both updraft and downdrafts. For example, the  $x$  component of updraft apparent momentum source ( $X_{xU}$ ) is positive and negative below and above 4-km height, respectively, with the maximum positive value at 3-km altitude for

$dx = 32\text{--}128$  km. The  $y$  component of updraft apparent momentum source ( $X_{yU}$ ) is negative below 6-km height but positive above 6-km height, with the minimum  $X_{yU}$  occurring at  $\sim 5$ -km altitude for  $dx = 32\text{--}256$  km. Further, apparent momentum source in updrafts is larger than that in downdrafts ( $X_{xD}$  and  $X_{yD}$ ).

As shown in Eq. (6), the apparent momentum source is composed of CIPG, vertical advection of horizontal momentum, and detrainment [the three terms on the right-hand side of Eq. (6)]. The magnitudes of these

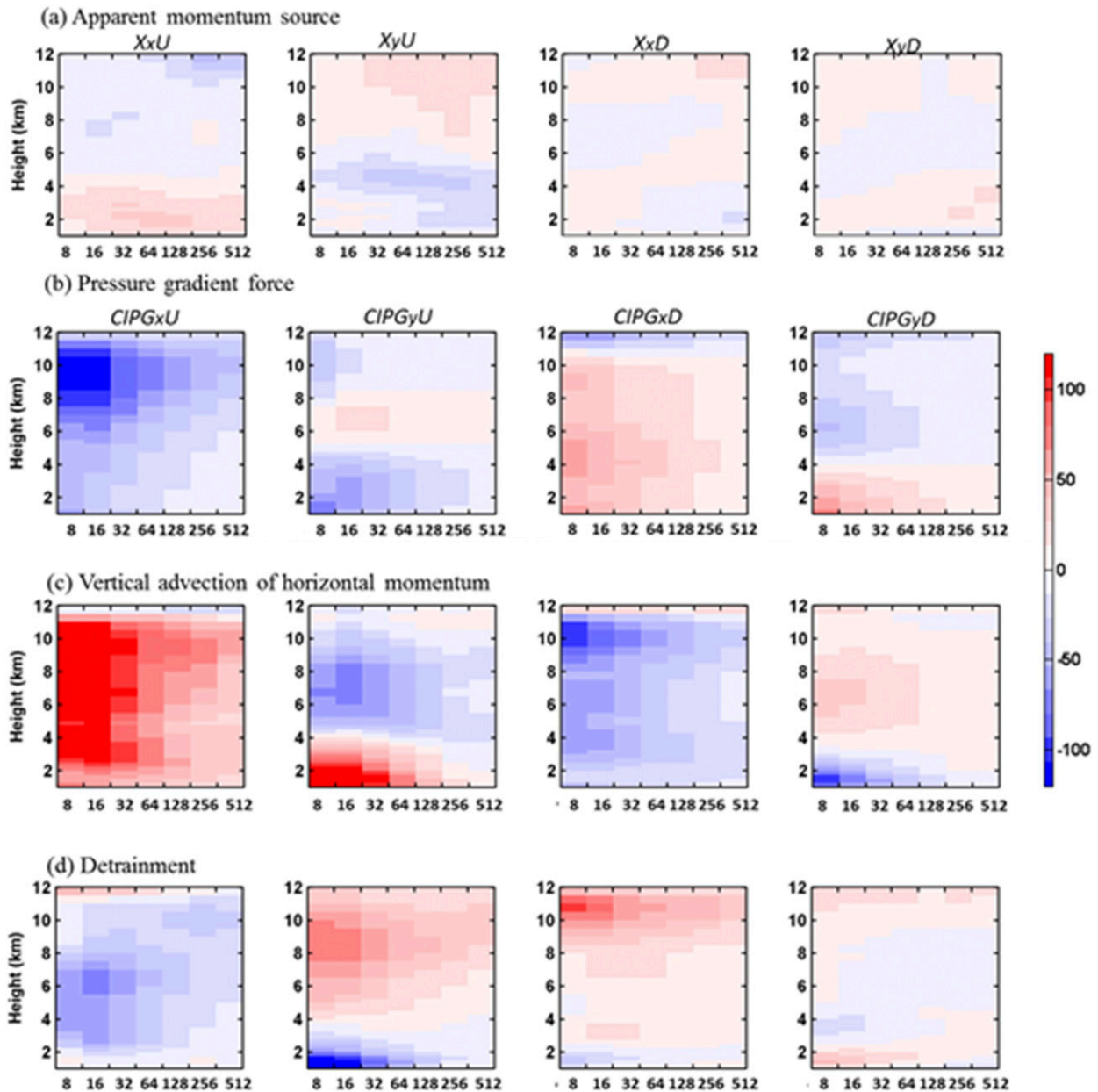


FIG. 12. Vertical profiles of scale dependency of (a) apparent momentum source ( $\text{m s}^{-1} \text{day}^{-1}$ ), (b) CIPG ( $\text{m s}^{-1} \text{day}^{-1}$ ), (c) vertical advection by the compensating subsidence ( $\text{m s}^{-1} \text{day}^{-1}$ ), and (d) horizontal momentum detrainment ( $\text{m s}^{-1} \text{day}^{-1}$ ) for MC3E-0523: (left to right)  $x$  component of updrafts,  $y$  component of updrafts,  $x$  component of downdrafts, and  $y$  component of downdrafts.

three terms are much larger than that of apparent momentum source. The vertical advection of horizontal momentum has a slightly larger magnitude than that of CIPG, and they are opposite in sign except for the updraft  $y$  component above 8-km altitude. The detrainment term is the smallest among the three terms. The magnitudes of CIPG and apparent momentum source are comparable at very large grid spacing such as 512 and 256 km. As grid spacing decreases, the

magnitude of CIPG increases more rapidly than that of apparent momentum source; thus, CIPG becomes significantly larger than apparent momentum source at small grid spacings. These results suggest that CIPG can have significant impacts on apparent momentum source at GCM resolution, and the impact may become even larger at the gray-zone resolution. Because of this finding, it is imperative to revisit the parameterization scheme for CIPG across all the scales.

To further understand the factors impacting the scale dependency of CIPG, vertical profiles of individual terms in the Laplacian of CIPG [Eq. (7)] are compared for different grid spacings (Figs. 13 and 14 and Figs. S8–S11). For MC3E-0523 (nonlinear MCS), contributions from the buoyancy, divergence, and stratification forcings to the Laplacian of CIPG are very small for all grid spacings (Fig. 13 and Figs. S8 and S9 in SI). Therefore, the discussion for MC3E-0523 will focus on the linear-shear and nonlinear-shear forcings below. For the  $x$  component of both updraft and downdraft Laplacian of CIPG, the absolute value of the linear-shear forcing increases monotonically with decreasing grid spacing and is the major contributor to the Laplacian of CIPG for all grid spacings (Figs. 13a,c). Although the linear-shear forcing has the same sign and similar vertical structures as the Laplacian of CIPG for all grid spacings, their differences in vertical profiles increase as the grid spacing increases.

Unlike the linear-shear forcing, the nonlinear-shear forcing has similar magnitudes across the grid spacings and in general has the opposite sign to the Laplacian of CIPG and the linear-shear forcing. Because the linear-shear forcing's absolute value monotonically decreases with increasing grid spacing, contribution from the nonlinear-shear forcing to the Laplacian of CIPG becomes noticeable at  $dx = 32$  km and becomes comparable to the linear-shear forcing in magnitude at grid spacings  $> 64$  km. This explains the increased difference with increased grid spacing between the linear-shear forcing and the Laplacian of CIPG.

Different from the  $x$  component for updraft and downdraft Laplacian of CIPG whose linear-shear forcing is always larger than the other four terms regardless of grid spacings, for the  $y$  component of updraft and downdraft Laplacian of CIPG (Figs. 13b,d), the nonlinear-shear forcing in its absolute value becomes larger than the linear-shear forcing at  $dx > 64$  km. In addition, the linear-shear forcing term does not always have the same sign as the Laplacian of CIPG when  $dx > 16$  km, in particular at  $dx = 256$  and  $512$  km.

For MC3E-0520 (linear MCS), contributions from the divergence and stratification forcings to the Laplacian of CIPG remain negligibly small (Fig. 14). For  $dx = 4$ – $64$  km, the  $x$  and  $y$  components of both updraft and downdraft linear-shear forcings in general have the same sign as the Laplacian of CIPG and are the major contributor to the Laplacian of CIPG. However, for  $dx = 128$ – $512$  km, contributions of the linear-shear, nonlinear-shear, and buoyancy forcings to the Laplacian of CIPG become comparable, and the linear-shear forcing sometimes has an opposite sign to the Laplacian of CIPG below the 6-km altitudes.

The CIPG budget analysis presented above suggests that for both linear and nonlinear MCSs, both the nonlinear-shear forcing and/or buoyancy forcing become comparable to the linear-shear forcing and sometimes exceed the linear-shear forcing as the grid spacing increase from 4–64- to 128–256-km although the linear-shear forcing is the major contributor to the Laplacian of CIPG for 4–64-km grid spacings. Thus, inclusion of the linear-shear forcing only to represent the Laplacian of CIPG such as in the **GKI97** scheme may be acceptable only at  $dx = 4$ – $64$  km where the magnitudes of other forcings are small.

#### *d. Scale dependency of parameterized CIPG by the **GKI97** scheme*

The **GKI97** scheme [Eq. (8)] only includes the linear-shear forcing term for parameterizing CIPG, that is, a constant coefficient multiplied by mass flux and vertical mean wind shear. The same constant coefficient is used in the  $x$  and  $y$  components of CIPG for updrafts and downdrafts. As revealed from Figs. 13 and 14, the relationship between CIPG and linear-shear forcing term can be different for the  $x$  and  $y$  components at different grid spacings. Thus, using the same coefficient for their  $x$  and  $y$  components across different grid spacings may cause significant errors. Although the stratification and divergence forcings are small and neglecting them is justifiable, contributions of both the nonlinear-shear and buoyancy forcings to CIPG are not negligible at  $dx > 64$  km. Thus, we suspect that exclusion of the nonlinear-shear forcing or buoyancy forcing in the parameterization of CIPG may impact the degree of accuracy. Therefore, in this section, we evaluate the performance of the **GKI97** scheme for parameterizing the CIPG for different grid spacings using the linear regression analysis at each level for different grid spacings.

Both MC3E-0520 and MC3E-0523 consistently show that at  $dx = 4$ – $128$  km, the  $x$ - and  $y$ -component CIPG and product of mass flux and vertical mean wind shear for updrafts and downdrafts [Eq. (8)] are negatively correlated at all levels, while for  $dx = 256$  and  $512$  km, they can be either positively or negatively correlated (Fig. 15 and Fig. S12). In addition,  $R_{\text{adj}}^2$  monotonically increases with increasing grid spacing at the 4–64-km range, in which the grid spacing of 64 km has the maximum  $R_{\text{adj}}^2$ . This suggests that the **GKI97** scheme may explain the most CIPG variation at  $dx = 64$  km, and at the smaller grid spacing, the less variation of CIPG can be captured by the **GKI97** scheme. In contrast, for  $dx > 64$  km, there is no such clear relation between  $R_{\text{adj}}^2$  and grid spacing, and  $R_{\text{adj}}^2$  varies greatly with height.

As for the regression slopes, it is shown that at the grid spacing ranging from 4 to 128 km, the range of the slope

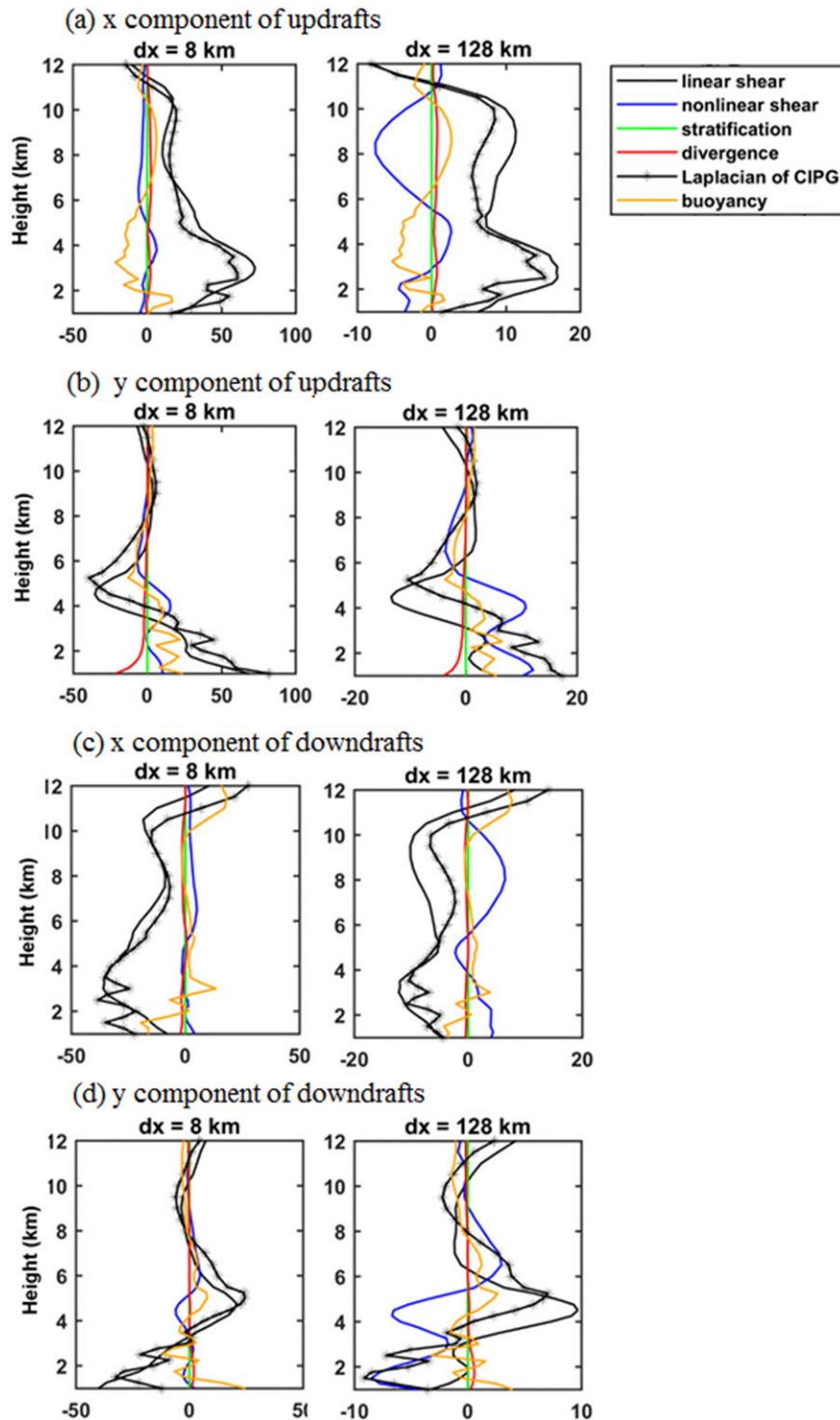


FIG. 13. Linear-shear forcing (black line;  $10^{-11} \text{ kg m}^{-4} \text{ s}^{-2}$ ), nonlinear-shear forcing (blue line;  $10^{-11} \text{ kg m}^{-4} \text{ s}^{-2}$ ), stratification forcing (green line;  $10^{-11} \text{ kg m}^{-4} \text{ s}^{-2}$ ), divergence forcing (red line;  $10^{-11} \text{ kg m}^{-4} \text{ s}^{-2}$ ), buoyancy forcing (yellow line;  $10^{-11} \text{ kg m}^{-4} \text{ s}^{-2}$ ), and the Laplacian of CIPG (black line with marks) over (a)  $x$  component of updrafts, (b)  $y$  component of updrafts, (c)  $x$  component of downdrafts, and (d)  $y$  component of downdrafts for MC3E-0523 for  $dx =$  (left) 8 and (right) 128 km. Please refer to Figs. S8 and S9 for the results of all different grid spacings.

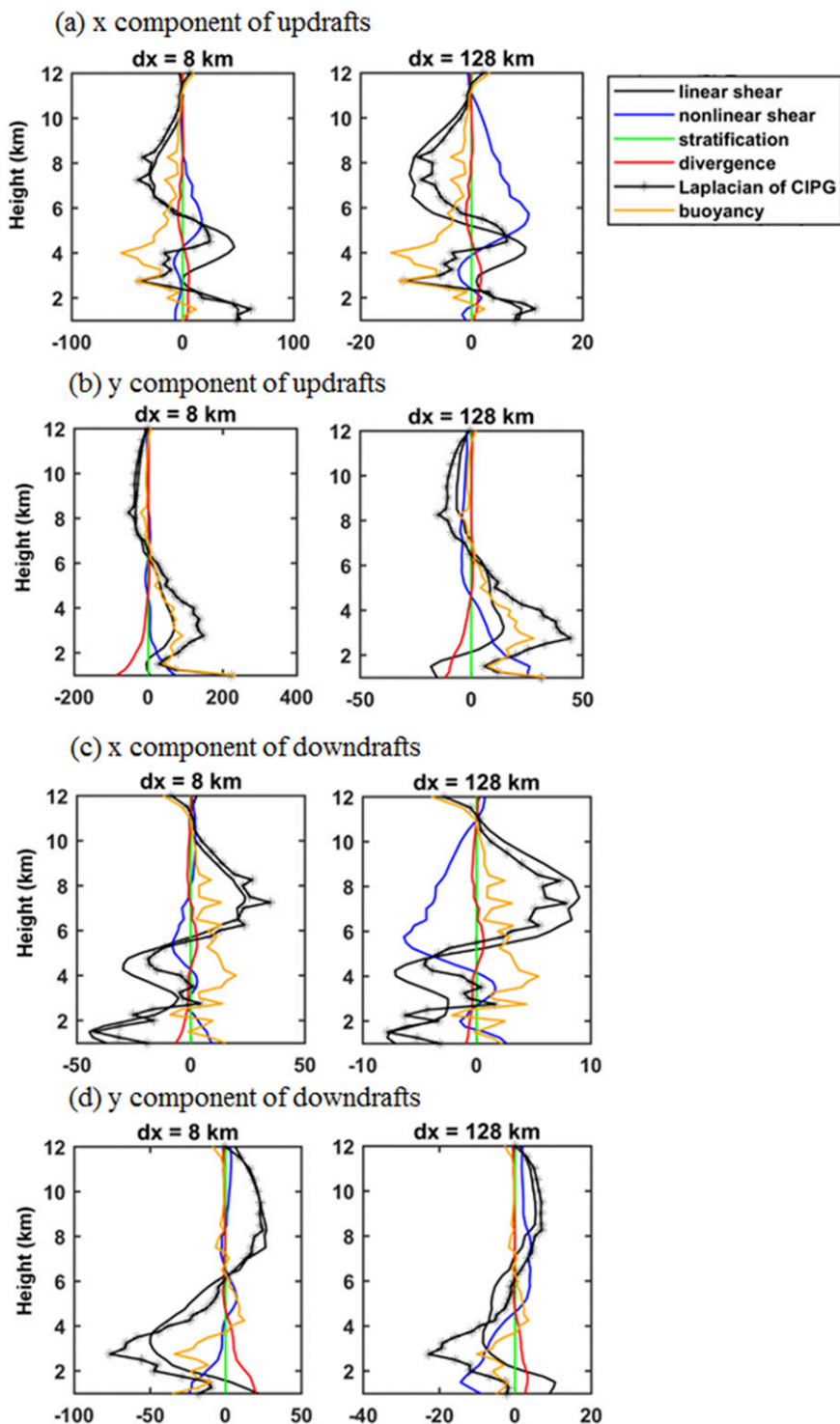


FIG. 14. As in Fig. 13, but for MC3E-0520. Please refer to Figs. S10 and S11 for the results of all different grid spacings.

variation in the vertical (1–12-km altitudes) tends to increase as grid spacing increases for both the  $x$  and  $y$  components of updrafts and downdrafts (Table 1 and Table S1 in SI). For example, for  $dx = 4$  km from

MC3E-0523, the  $x$  component of updraft slopes ranges from  $-0.44$  to  $-0.24$ , and for  $dx = 128$  km, they range from  $-0.47$  to  $-0.07$ . However, the mean slopes averaged over 1–12-km altitude do not vary much with grid

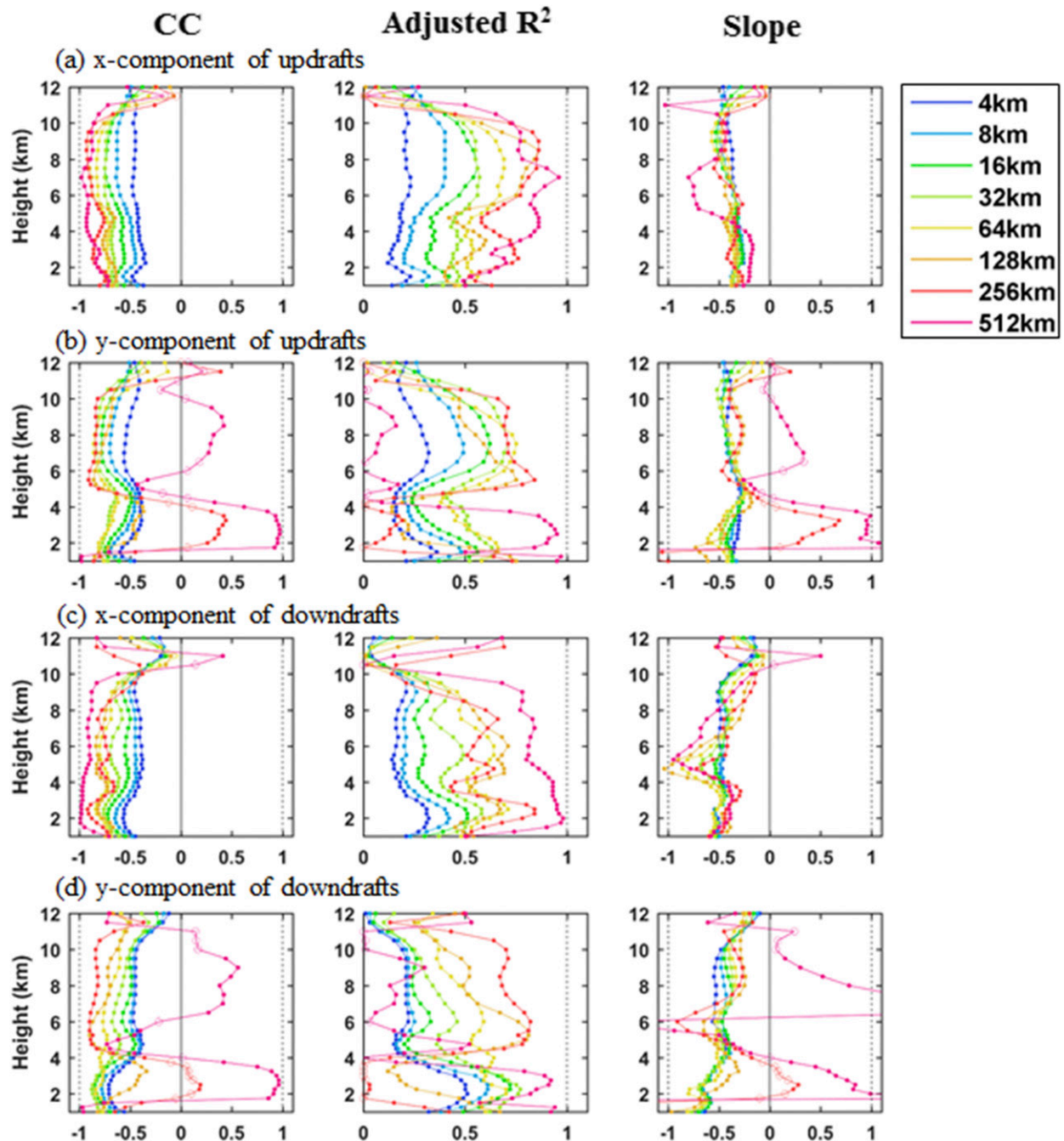


FIG. 15. Vertical profiles of (left to right) Pearson CC, adjusted coefficient of determination ( $R_{\text{adj}}^2$ ), and linear regression slope between CIPG and the product of mass flux and the vertical mean wind shear for (a)  $x$  component of updrafts, (b)  $y$  component of updrafts, (c)  $x$  component of downdrafts, and (d)  $y$  component of downdrafts from MC3E-0523. The open circles indicate where the CC  $R_{\text{adj}}^2$  and linear regression slope are statistically insignificant.

spacings. The mean slopes are ranging from  $-0.32$  to  $-0.37$  across the grid spacings for the  $x$  component of updraft slopes, from  $-0.32$  to  $-0.41$  for the  $y$  component of updrafts slopes, from  $-0.45$  to  $-0.49$  for the  $x$  component of downdraft slopes, and from  $-0.49$  to  $-0.52$  for

the  $y$  component of downdraft slopes. Since the mean regression slope does not vary much with grid spacing for the same component, we take vertical averages. The average slope is  $-0.35$  for the  $x$  component of updraft slope,  $-0.39$  for the  $y$  component of updraft slope,  $-0.47$

TABLE 1. The minimum, maximum, and average  $x$  component of updraft slopes ( $xU$ ),  $y$  component of updraft slopes ( $yU$ ),  $x$  component of downdraft slopes ( $xD$ ), and  $y$  component of downdraft slopes ( $yD$ ) between 1- and 12-km heights for selected grid spacings from MC3E-0523 and MC3E-0520. For the results of all different grid spacings, please refer to Table S1.

$dx$ (km)	$xU$			$yU$			$xD$			$yD$		
	Min	Max	Avg									
MC3E-0523												
8	-0.5	-0.22	-0.34	-0.48	-0.27	-0.38	-0.55	-0.16	-0.45	-0.67	-0.14	-0.49
128	-0.47	-0.07	-0.33	-0.62	-0.05	-0.32	-1.04	-0.07	-0.45	-0.9	-0.22	-0.51
MC3E-0520												
8	-0.38	-0.17	-0.26	-0.54	-0.13	-0.39	-0.68	-0.28	-0.51	-0.63	-0.3	-0.48
128	-0.36	-0.12	-0.22	-0.86	0.25	-0.45	-0.48	-0.05	-0.32	-0.78	0.28	-0.23

for the  $x$  component of downdraft slope, and  $-0.50$  for the  $y$  component of downdraft slope from MC3E-0523 (Table 2). The average slopes for MC3E-0520 are also listed in Table 2. It appears that the average slopes are different for different cases. In general, the average slopes appear to be larger for downdrafts than updrafts.

In summary, the two cases consistently demonstrate that the GKI97 scheme is satisfactory to a first-order approximation of parameterized CIPG for climate models with grid size  $< 64$  km. However, the variations of CIPG that can be captured using the GKI97 scheme decrease when grid spacing increases. When grid spacing is at 128 km or larger, the GKI97 scheme does not fully parameterize CIPG. This behavior is related to the fact that GKI97 only considers the contribution from linear forcing but does not consider the contribution from the nonlinear-shear forcing or buoyancy forcing, which can become comparable or even larger than the linear-shear forcing when  $dx > 64$  km. It is surprising that the GKI97 scheme is actually not suitable when the model grid spacing is at the traditional GCM scales (100–300 km). This might explain why Richter and Rasch (2008), which used horizontal resolutions of  $1.9^\circ$  and  $2.5^\circ$ , obtained better result from the SL76 scheme that did not consider the effect of CIPG than that from the GKI97 scheme that includes the CIPG effect.

To investigate whether adding the nonlinear-shear forcing into the GKI97 scheme can potentially improve the ability for capturing the variation of CIPG, we conduct a multiple linear regression analysis using two predictor variables, including the product of mass flux and vertical mean wind shear (GKI97; linear-shear forcing) and the product of mass flux and vertical perturbation wind shear (nonlinear-shear forcing). It is shown that when nonlinear-shear term is added into the regression equation,  $R_{adj}^2$  value increases significantly at  $dx = 128$ – $512$  km (Fig. 16). However, the increase of  $R_{adj}^2$  value at  $dx < 100$  km is much smaller compared to that

at  $dx > 100$  km. This confirms that adding the nonlinear forcing to the GKI97 scheme might potentially improve the predictability of CIPG for  $dx > 100$  km, while the improvement is limited for  $dx < 100$  km. A potentially better way to parameterize the CIPG at the grid spacing range from 4 to 64 km would still use the GKI97 scheme but with a modification that can capture the large inter-draft variability in convective updraft area within a grid box. This may be achieved by using the three-updrafts and one-downdraft approach (Liu et al. 2015), which shows much improved CMT compared to the traditional single updraft and downdraft approach as shown in Fig. 17 because it well accounts for the increasing variation inside convection at the gray-zone scale.

## 5. Summary and discussion

This study has focused on diagnosing and exploring the scale dependency of convective momentum transport (CMT) and CMT-related properties and evaluating the convection-induced pressure gradient (CIPG) parameterization in GKI97. A statistical ensemble method is used to analyze the 3D Weather Research and Forecasting (WRF) Model simulations at the cloud-permitting scale for two midlatitude convective systems (i.e., a mesoscale convective complex and a squall line observed during the MC3E field experiment).

The two CRM-simulated cases consistently show that the grid-mean wind patterns generally do not change much with the change of grid spacings except for the  $y$

TABLE 2. The mean of average  $x$  component of updraft slopes ( $xU$ ),  $y$  component of updraft slopes ( $yU$ ),  $x$  component of downdraft slopes ( $xD$ ), and  $y$  component of downdraft slopes ( $yD$ ) from Table S1 for MC3E-0523 and MC3E-0520.

	$xU$	$yU$	$xD$	$yD$
MC3E-0523	-0.35	-0.39	-0.47	-0.50
MC3E-0520	-0.27	-0.41	-0.42	-0.47

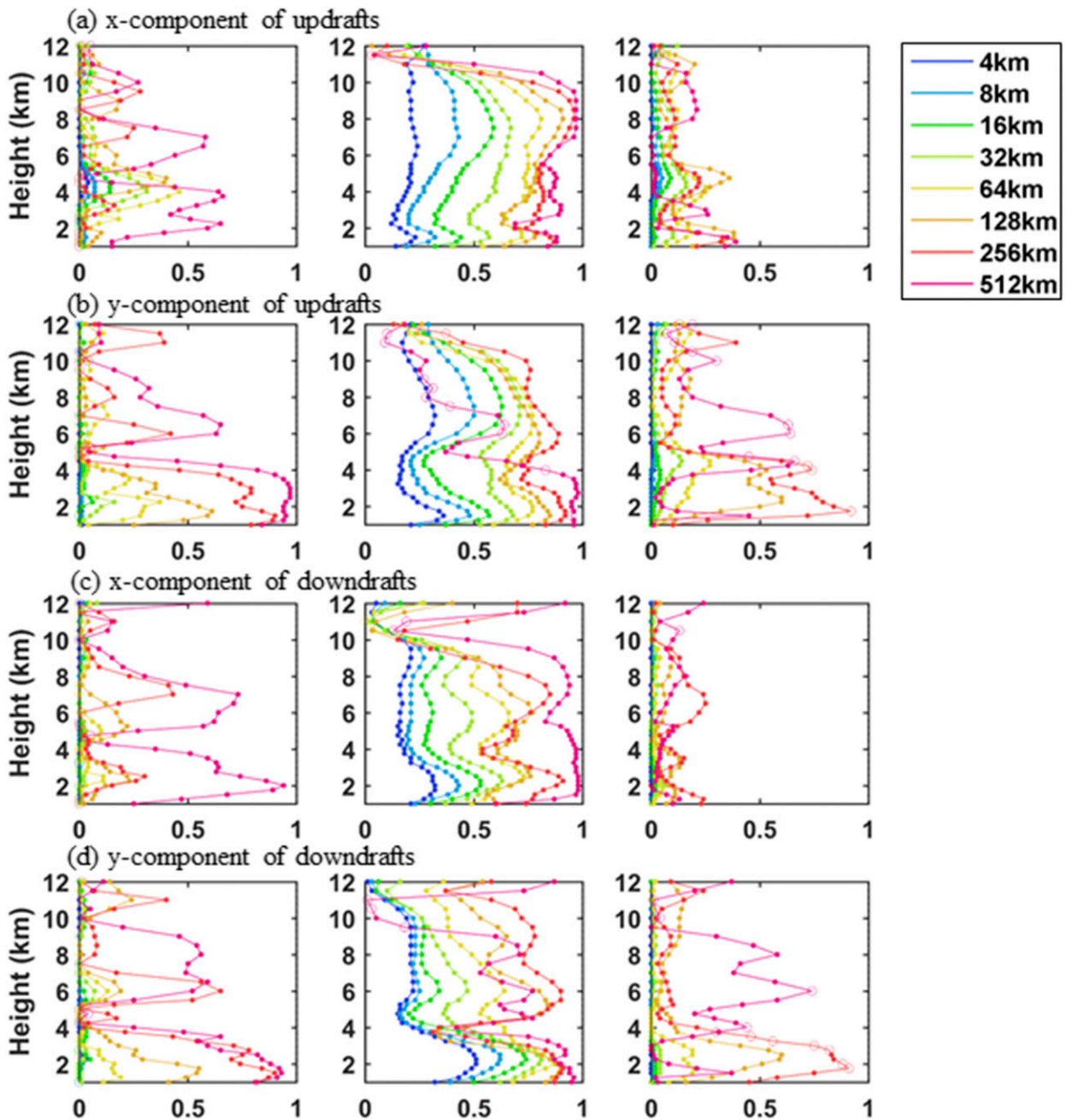


FIG. 16. As in Fig. 15, but for  $R_{\text{adj}}^2$ : (left) the product of mass flux and vertical perturbation wind shear and (middle) the combination of product of mass flux and vertical mean wind shear, as well as the product of mass flux and vertical perturbation wind shear, as predictor variables with CIPG as the response variable. (right) The difference in  $R_{\text{adj}}^2$  between the middle columns in Figs. 15 and 16.

component of the linear MCS. In contrast, updraft and downdraft mass fluxes and CMTs have strong scale dependency in temporal evolution and vertical structure. However, even with strong scale dependency, updraft CMT has the same sign from the small grid spacings to the large grid spacings, while downdraft CMT can have different signs between the small and large grid spacings.

Previous studies suggest that CMT is generally downgradient for nonlinear MCSs, but for linear MCSs, the CMT can be either upgradient or downgradient transports. We find that the prevalent CMT characteristics based upon field campaigns and model calculation for spatial scales typical of current GCM resolution are applicable to updrafts but not downdrafts across a wide

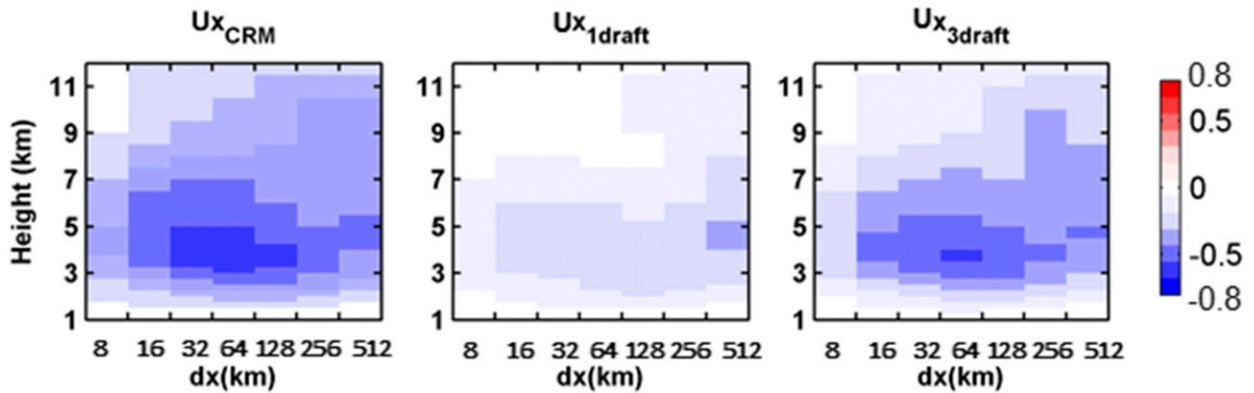


FIG. 17. (left to right) Vertical profiles of the scale dependency of the  $x$  component of updraft vertical momentum flux ( $\text{kg m}^{-1} \text{s}^{-2}$ ) from CRM, the one-updraft approach, and the three-updraft approach for MC3E-0523. Please refer to Figs. S14 and S15 for the results of  $x$  and  $y$  components of updraft, downdraft, environment, and total vertical momentum fluxes.

range of grid spacings. Total and updraft CMT for the nonlinear MCSs (MC3E-0523) are mostly downgradient with respect to grid-mean wind shear at all levels for both the small and large grid spacings. Updraft and total CMT for the linear MCS (MC3E-0520) also consistently show downgradient transport in the line-parallel direction and upgradient transport in the line-normal direction for both large grid spacings at all levels and small grid spacings below 7-km altitude. In contrast, downdraft CMT for nonlinear MCSs is upgradient at the large grid spacings and becomes downgradient at the small grid spacings. For linear MCS, downdraft CMT is mostly downgradient for both the  $x$  and  $y$  components at both the small and large spacings.

We also investigate why linear MCS has downgradient updraft CMT in the  $x$  direction but upgradient CMT in the  $y$  direction for both large and small grid spacings. For the upgradient CMT in the  $y$  direction, the reason is that the updraft pressure gradient force (PGF) strengthens perturbation wind in updrafts for both the large and small grid spacings. In contrast, in the  $x$  direction, the updraft PGF weakens perturbation wind inside updrafts, resulting in downgradient CMT. However, downdraft CMT shows no clear relation to downdraft PGF.

The analyses of scale dependency of apparent momentum source suggest that CIPG has significant impacts on apparent momentum source at GCM resolution, and the influence becomes even larger at the gray-zone resolution. Further analysis of the individual components for the Laplacian of CIPG shows that although linear-shear forcing is the major contributor to the  $x$  component of updraft and downdraft Laplacian of CIPG for all the grid spacings from MC3E-0523, the contribution of nonlinear-shear forcing to the  $y$  component of updraft and downdraft Laplacian of

CIPG from MC3E-0523 as well as both the  $x$  and  $y$  components of Laplacian of CIPG from MC3E-0520 can be comparable and even exceeds the linear-shear forcing at grid spacing larger than 64 km. This suggest that use of only the linear-shear forcing for representing the Laplacian of CIPG might be acceptable only at  $dx = 4\text{--}64$  km either when convective-scale effect dominates or when the mesoscale circulation is absent. However, when grid spacing is large, the effect of MCS organization will inevitably be included in each grid box; thus, the inclusion of the nonlinear-shear forcing becomes important (Badlan et al. 2017).

We have also evaluated one of the most widely used CMT parameterization schemes in GCMs that included the effect of CIPG (Wu and Yanai 1994; GKI97; Badlan et al. 2017). We performed the linear regression analysis between the CIPG and the product of mass flux and vertical mean wind shear at each level to quantify the performance of the GKI97 scheme across different grid spacings. Results show that  $R_{\text{adj}}^2$  monotonically increases with increasing grid spacing at the grid spacing range between 4 and 64 km, in which the grid spacing of 64 km has the maximum  $R_{\text{adj}}^2$ . This suggests that the GKI97 scheme may explain the most CIPG variation at grid spacing of 64 km, and at the smaller grid spacing, the less variation of CIPG can be captured by the GKI97 scheme. Based on the multiple-variable regression analysis, the ability to capture the increasing variation of CIPG with decreasing grid spacing cannot be improved with the inclusion of nonlinear-shear forcing as another predictor. Thus, a better way to parameterize the convection-induced pressure gradient at the grid spacing range from 4 to 64 km would still use the GKI97 scheme but with a modification that can capture the large inter-draft variability in convective updraft area within a grid

box. This may be achieved by using the three-updraft approach (Liu et al. 2015), which can well account for the increasing variation inside convection at the gray-zone scale compared to the traditional single updraft and downdraft approach.

We also found that when grid spacing increases to 128 km or larger, the negative correlation between CIPG and the linear-shear forcing would somehow break down and becomes highly sensitive to altitudes. This is because the GKI97 scheme does not consider the contribution from the nonlinear-shear forcing and buoyancy forcing, which can be comparable or even larger than the linear-shear forcing when  $\Delta x$  is larger than 100 km. This finding suggests that the GKI97 parameterization for CIPG is actually not suitable for model grid spacing at the traditional GCM scales (100–300 km) unless the nonlinear forcing is included.

*Acknowledgments.* Support for this work was provided by Scientific Discovery through Advanced Computing (SciDAC) program funded by U.S. Department of Energy Office of Advanced Scientific Computing Research and Office of Biological and Environmental Research. The Pacific Northwest National Laboratory (PNNL) is operated for the DOE by Battelle Memorial Institute under Contract DE-AC06-76RLO 1830. Kuan-Man Xu was supported by NASA Modeling, Analysis and Prediction program. Guang J. Zhang was supported by the PNNL SciDAC Subcontract DOE/PNNL 190110. The data used in this study were produced by Pacific Northwest National Laboratory and are stored on PNNL Olympus. They are available upon request by contacting the corresponding author.

#### REFERENCES

- Arakawa, A., and C.-M. Wu, 2013: A unified representation of deep moist convection in numerical modeling of the atmosphere. Part I. *J. Atmos. Sci.*, **70**, 1977–1992, <https://doi.org/10.1175/JAS-D-12-0330.1>.
- , J.-H. Jung, and C.-M. Wu, 2011: Toward unification of the multiscale modeling of the atmosphere. *Atmos. Chem. Phys.*, **11**, 3731–3742, <https://doi.org/10.5194/acp-11-3731-2011>.
- Asai, T., 1970: Three-dimensional features of thermal convection in a plane Couette flow. *J. Meteor. Soc. Japan*, **48**, 18–29, [https://doi.org/10.2151/jmsj1965.48.1\\_18](https://doi.org/10.2151/jmsj1965.48.1_18).
- Badlan, R. L., T. P. Lane, M. W. Moncrieff, and C. Jakob, 2017: Insights into convective momentum transport and its parameterization from idealized simulations of organized convection. *Quart. J. Roy. Meteor. Soc.*, **143**, 2687–2702, <https://doi.org/10.1002/qj.3118>.
- Cheng, A., and K.-M. Xu, 2014: An explicit representation of vertical momentum transport in a multiscale modeling framework through its 2-D cloud-resolving model component. *J. Geophys. Res. Atmos.*, **119**, 2356–2374, <https://doi.org/10.1002/2013JD021078>.
- Deng, L., and X. Wu, 2010: Effects of convective processes on GCM simulations of the Madden–Julian oscillation. *J. Climate*, **23**, 352–377, <https://doi.org/10.1175/2009JCLI3114.1>.
- Fan, J., L. R. Leung, Z. Li, H. Morrison, H. Chen, Y. Zhou, Y. Qian, and Y. Wang, 2012: Aerosol impacts on clouds and precipitation in eastern China: Results from bin and bulk microphysics. *J. Geophys. Res.*, **117**, D00K36, <https://doi.org/10.1029/2011JD016537>.
- , and Coauthors, 2015: Improving representation of convective transport for scale-aware parameterization: 1. Convection and cloud properties simulated with spectral bin and bulk microphysics. *J. Geophys. Res. Atmos.*, **120**, 3485–3509, <https://doi.org/10.1002/2014JD022142>.
- Gallus, W. A., Jr., and R. H. Johnson, 1992: The momentum budget of an intense midlatitude squall line. *J. Atmos. Sci.*, **49**, 422–450, [https://doi.org/10.1175/1520-0469\(1992\)049<0422:TMBOAI>2.0.CO;2](https://doi.org/10.1175/1520-0469(1992)049<0422:TMBOAI>2.0.CO;2).
- Grabowski, W. W., and M. W. Moncrieff, 2001: Large-scale organization of tropical convection in two-dimensional explicit numerical simulations. *Quart. J. Roy. Meteor. Soc.*, **127**, 445–468, <https://doi.org/10.1002/qj.49712757211>.
- Gregory, D., R. Kershaw, and P. M. Inness, 1997: Parameterization of momentum transport by convection. II: Tests in single-column and general circulation models. *Quart. J. Roy. Meteor. Soc.*, **123**, 1153–1183, <https://doi.org/10.1002/qj.49712354103>.
- Han, J., and H.-L. Pan, 2006: Sensitivity of hurricane intensity forecast to convective momentum transport parameterization. *Mon. Wea. Rev.*, **134**, 664–674, <https://doi.org/10.1175/MWR3090.1>.
- Helfand, H. M., 1979: The effect of cumulus friction on the simulation of the January Hadley circulation by the GLAS model of the general circulation. *J. Atmos. Sci.*, **36**, 1827–1843, [https://doi.org/10.1175/1520-0469\(1979\)036<1827:TEOCFO>2.0.CO;2](https://doi.org/10.1175/1520-0469(1979)036<1827:TEOCFO>2.0.CO;2).
- Houze, R. A., Jr., 1973: A climatological study of vertical transports by cumulus-scale convection. *J. Atmos. Sci.*, **30**, 1112–1123, [https://doi.org/10.1175/1520-0469\(1973\)030<1112:ACSOVT>2.0.CO;2](https://doi.org/10.1175/1520-0469(1973)030<1112:ACSOVT>2.0.CO;2).
- , S. S. Chen, D. E. Kingsmill, Y. Serra, and S. E. Yuter, 2000: Convection over the Pacific warm pool in relation to the atmospheric Kelvin–Rossby wave. *J. Atmos. Sci.*, **57**, 3058–3089, [https://doi.org/10.1175/1520-0469\(2000\)057<3058:COTPPW>2.0.CO;2](https://doi.org/10.1175/1520-0469(2000)057<3058:COTPPW>2.0.CO;2).
- Khain, A., A. Pokrovsky, M. Pinsky, A. Seifert, and V. Phillips, 2004: Simulation of effects of atmospheric aerosols on deep turbulent convective clouds using a spectral microphysics mixed-phase cumulus cloud model. Part I: Model description and possible applications. *J. Atmos. Sci.*, **61**, 2963–2982, <https://doi.org/10.1175/JAS-3350.1>.
- Khairoutdinov, M. F., and D. A. Randall, 2001: A cloud resolving model as a cloud parameterization in the NCAR Community Climate Model: Preliminary results. *Geophys. Res. Lett.*, **28**, 3617–3620, <https://doi.org/10.1029/2001GL013552>.
- Khouider, B., Y. Han, and J. A. Biello, 2012a: Convective momentum transport in a simple multicloud model for organized convection. *J. Atmos. Sci.*, **69**, 281–302, <https://doi.org/10.1175/JAS-D-11-042.1>.
- , —, A. J. Majda, and S. N. Stechmann, 2012b: Multiscale waves in an MJO background and convective momentum transport feedback. *J. Atmos. Sci.*, **69**, 915–933, <https://doi.org/10.1175/JAS-D-11-0152.1>.
- Lane, T. P., and M. W. Moncrieff, 2010: Characterization of momentum transport associated with organized moist convection

- and gravity waves. *J. Atmos. Sci.*, **67**, 3208–3225, <https://doi.org/10.1175/2010JAS3418.1>.
- LeMone, M. A., 1983: Momentum transport by a line of cumulonimbus. *J. Atmos. Sci.*, **40**, 1815–1834, [https://doi.org/10.1175/1520-0469\(1983\)040<1815:MTBALO>2.0.CO;2](https://doi.org/10.1175/1520-0469(1983)040<1815:MTBALO>2.0.CO;2).
- , and D. P. Jorgensen, 1991: Precipitation and kinematic structure of an oceanic mesoscale convective system. Part I: Momentum transport and generation. *Mon. Wea. Rev.*, **119**, 2638–2653, [https://doi.org/10.1175/1520-0493\(1991\)119<2638:PAKSOA>2.0.CO;2](https://doi.org/10.1175/1520-0493(1991)119<2638:PAKSOA>2.0.CO;2).
- , and M. W. Moncrieff, 1994: Momentum and mass transport by convective bands: Comparisons of highly idealized dynamical models to observations. *J. Atmos. Sci.*, **51**, 281–305, [https://doi.org/10.1175/1520-0469\(1994\)051<0281:MAMTBC>2.0.CO;2](https://doi.org/10.1175/1520-0469(1994)051<0281:MAMTBC>2.0.CO;2).
- , G. M. Barnes, and E. J. Zipser, 1984: Momentum flux by lines of cumulonimbus over the tropical ocean. *J. Atmos. Sci.*, **41**, 1914–1932, [https://doi.org/10.1175/1520-0469\(1984\)041<1914:MFBLOC>2.0.CO;2](https://doi.org/10.1175/1520-0469(1984)041<1914:MFBLOC>2.0.CO;2).
- Liu, Y.-C., J. Fan, G. J. Zhang, K.-M. Xu, and S. J. Ghan, 2015: Improving representation of convective transport for scale-aware parameterization: 2. Analysis of cloud-resolving model simulations. *J. Geophys. Res. Atmos.*, **120**, 3510–3532, <https://doi.org/10.1002/2014JD022145>.
- Majda, A. J., and S. N. Stechmann, 2008: Stochastic models for convective momentum transport. *Proc. Natl. Acad. Sci. USA*, **105**, 17 614–17 619, <https://doi.org/10.1073/pnas.0806838105>.
- , and —, 2009: A simple dynamical model with features of convective momentum transport. *J. Atmos. Sci.*, **66**, 373–392, <https://doi.org/10.1175/2008JAS2805.1>.
- , and —, 2016: Models for multiscale interactions. Part II: Madden–Julian oscillation, moisture, and convective momentum transport. *Multiscale Convection-Coupled Systems in the Tropics: A Tribute to Dr. Michio Yanai, Meteor. Monogr.*, No. 56, Amer. Meteor. Soc., 10.1–10.5, <https://doi.org/10.1175/AMSMONOGRAPHS-D-15-0005.1>.
- Moncrieff, M. W., 1981: A theory of organized steady convection and its transport properties. *Quart. J. Roy. Meteor. Soc.*, **107**, 29–50, <https://doi.org/10.1002/qj.49710745103>.
- , 1992: Organized convective systems: Archetypal dynamical models, mass and momentum flux theory, and parametrization. *Quart. J. Roy. Meteor. Soc.*, **118**, 819–850, <https://doi.org/10.1002/qj.49711850703>.
- , and J. S. A. Green, 1972: The propagation and transfer properties of steady convective overturning in shear. *Quart. J. Roy. Meteor. Soc.*, **98**, 336–352, <https://doi.org/10.1002/qj.49709841607>.
- , and C. Liu, 2006: Representing convective organization in prediction model by a hybrid strategy. *J. Atmos. Sci.*, **63**, 3404–3420, <https://doi.org/10.1175/JAS3812.1>.
- Neale, R. B., and Coauthors, 2010: Description of the NCAR Community Atmosphere Model (CAM5). NCAR Tech. Note NCAR/TN-486+STR, 268 pp., [www.cesm.ucar.edu/models/cesm1.1/cam/docs/description/cam5\\_desc.pdf](http://www.cesm.ucar.edu/models/cesm1.1/cam/docs/description/cam5_desc.pdf).
- Ooyama, K., 1971: A theory on parameterization of cumulus convection. *J. Meteor. Soc. Japan*, **49**, 744–756, [https://doi.org/10.2151/jmsj1965.49A.0\\_744](https://doi.org/10.2151/jmsj1965.49A.0_744).
- Petersen, W. A., and M. Jensen, 2012: The NASA-GPM and DOE-ARM Midlatitude Continental Convective Clouds Experiment (MC3E). *The Earth Observer*, Vol. 24, No. 1, NASA GSFC Science Communications Support Office, Greenbelt, Maryland, 12–18, [https://eosppo.nasa.gov/sites/default/files/eo\\_pdfs/Jan\\_Feb\\_2012\\_col\\_508.pdf](https://eosppo.nasa.gov/sites/default/files/eo_pdfs/Jan_Feb_2012_col_508.pdf).
- Richter, J. H., and P. J. Rasch, 2008: Effects of convective momentum transport on the atmospheric circulation in the Community Atmosphere Model, version 3. *J. Climate*, **21**, 1487–1499, <https://doi.org/10.1175/2007JCLI1789.1>.
- Romps, D. M., 2012: On the equivalence of two schemes for convective momentum transport. *J. Atmos. Sci.*, **69**, 3491–3500, <https://doi.org/10.1175/JAS-D-12-068.1>.
- Rotunno, R., and J. B. Klemp, 1982: The influence of the shear-induced pressure gradient on thunderstorm motion. *Mon. Wea. Rev.*, **110**, 136–151, [https://doi.org/10.1175/1520-0493\(1982\)110<0136:TIOTSI>2.0.CO;2](https://doi.org/10.1175/1520-0493(1982)110<0136:TIOTSI>2.0.CO;2).
- Schneider, E. K., and R. S. Lindzen, 1976: A discussion of the parameterization of momentum exchange by cumulus convection. *J. Geophys. Res.*, **81**, 3158–3161, <https://doi.org/10.1029/JC081i018p03158>.
- Shapiro, L. J., and D. E. Stevens, 1980: Parameterization of convective effects on the momentum and vorticity budgets of synoptic-scale Atlantic tropical waves. *Mon. Wea. Rev.*, **108**, 1816–1826, [https://doi.org/10.1175/1520-0493\(1980\)108<1816:POCEOT>2.0.CO;2](https://doi.org/10.1175/1520-0493(1980)108<1816:POCEOT>2.0.CO;2).
- Shaw, T. A., and T. P. Lane, 2013: Toward an understanding of vertical momentum transports in cloud-system-resolving model simulations of multiscale tropical convection. *J. Atmos. Sci.*, **70**, 3231–3247, <https://doi.org/10.1175/JAS-D-13-068.1>.
- Song, X., X. Wu, G. J. Zhang, and R. W. Arritt, 2008: Dynamical effects of convective momentum transports on global climate simulations. *J. Climate*, **21**, 180–194, <https://doi.org/10.1175/2007JCLI1848.1>.
- Sui, C.-H., and M. Yanai, 1986: Cumulus ensemble effects on the large-scale vorticity and momentum fields of GATE. Part I: Observational evidence. *J. Atmos. Sci.*, **43**, 1618–1642, [https://doi.org/10.1175/1520-0469\(1986\)043<1618:CEEOTL>2.0.CO;2](https://doi.org/10.1175/1520-0469(1986)043<1618:CEEOTL>2.0.CO;2); Corrigendum, **46**, 1630, [https://doi.org/10.1175/1520-0469\(1989\)046<1630:C>2.0.CO;2](https://doi.org/10.1175/1520-0469(1989)046<1630:C>2.0.CO;2).
- Tollerud, E. I., and S. K. Esbensen, 1983: An observational study of the upper-tropospheric vorticity fields in GATE cloud clusters. *Mon. Wea. Rev.*, **111**, 2161–2175, [https://doi.org/10.1175/1520-0493\(1983\)111<2161:AOSOTU>2.0.CO;2](https://doi.org/10.1175/1520-0493(1983)111<2161:AOSOTU>2.0.CO;2).
- Tulich, S. N., 2015: A strategy for representing the effects of convective momentum transport in multiscale models: Evaluation using a new superparameterized version of the Weather Research and Forecast Model (SP-WRF). *J. Adv. Model. Earth Syst.*, **7**, 938–962, <https://doi.org/10.1002/2014MS000417>.
- Tung, W.-W., and M. Yanai, 2002a: Convective momentum transport observed during the TOGA COARE IOP. Part I: General features. *J. Atmos. Sci.*, **59**, 1857–1871, [https://doi.org/10.1175/1520-0469\(2002\)059<1857:CMTODT>2.0.CO;2](https://doi.org/10.1175/1520-0469(2002)059<1857:CMTODT>2.0.CO;2).
- , and —, 2002b: Convective momentum transport observed during the TOGA COARE IOP. Part II: Case studies. *J. Atmos. Sci.*, **59**, 2535–2549, [https://doi.org/10.1175/1520-0469\(2002\)059<2535:CMTODT>2.0.CO;2](https://doi.org/10.1175/1520-0469(2002)059<2535:CMTODT>2.0.CO;2).
- Wang, Y., J. Fan, R. Zhang, L. R. Leung, and C. Franklin, 2013: Improving bulk microphysics parameterizations in simulations of aerosol effects. *J. Geophys. Res. Atmos.*, **118**, 5361–5379, <https://doi.org/10.1002/jgrd.50432>.
- Wu, C.-M., and A. Arakawa, 2014: A unified representation of deep moist convection in numerical modeling of the atmosphere. Part II. *J. Atmos. Sci.*, **71**, 2089–2103, <https://doi.org/10.1175/JAS-D-13-0382.1>.
- Wu, X., and M. Yanai, 1994: Effects of vertical wind shear on the cumulus transport of momentum: Observations and parameterization. *J. Atmos. Sci.*, **51**, 1640–1660, [https://doi.org/10.1175/1520-0469\(1994\)051<1640:EOVWSO>2.0.CO;2](https://doi.org/10.1175/1520-0469(1994)051<1640:EOVWSO>2.0.CO;2).

- , X. Liang, and G. J. Zhang, 2003: Seasonal migration of ITCZ precipitation across the equator: Why can't GCMs simulate it? *Geophys. Res. Lett.*, **30**, 1824, <https://doi.org/10.1029/2003GL017198>.
- Zhang, G. J., and H. R. Cho, 1991a: Parameterization of the vertical transport of momentum by cumulus clouds. Part I: Theory. *J. Atmos. Sci.*, **48**, 1483–1492, [https://doi.org/10.1175/1520-0469\(1991\)048<1483:POTVTO>2.0.CO;2](https://doi.org/10.1175/1520-0469(1991)048<1483:POTVTO>2.0.CO;2).
- , and —, 1991b: Parameterization of the vertical transport of momentum by cumulus clouds. Part II: Application. *J. Atmos. Sci.*, **48**, 2448–2457, [https://doi.org/10.1175/1520-0469\(1991\)048<2448:POTVTO>2.0.CO;2](https://doi.org/10.1175/1520-0469(1991)048<2448:POTVTO>2.0.CO;2).
- , and N. A. McFarlane, 1995: Role of convective-scale momentum transport in climate simulation. *J. Geophys. Res.*, **100**, 1417–1426, <https://doi.org/10.1029/94JD02519>.
- , and X. Wu, 2003: Convective momentum transport and perturbation pressure field from a cloud-resolving model simulation. *J. Atmos. Sci.*, **60**, 1120–1139, [https://doi.org/10.1175/1520-0469\(2003\)060<1120:CMTAPP>2.0.CO;2](https://doi.org/10.1175/1520-0469(2003)060<1120:CMTAPP>2.0.CO;2).